

**Climate Dynamics manuscript No.**  
(will be inserted by the editor)

---

**1   Forced summer stationary waves: the opposing effects of  
2   direct radiative forcing and sea surface warming**

**3   Hugh S. Baker · Tim Woollings · Cheikh**

**4   Mbengue · Myles R. Allen · Christopher H.**

**5   O'Reilly · Hideo Shiogama · Sarah Sparrow**

**6   Received: date / Accepted: date**

---

H. S. Baker

Atmospheric, Oceanic and Planetary Physics, University of Oxford, Parks Rd, Oxford OX1 3PU, UK

Tel.: +441865 272912

E-mail: hugh.baker@physics.ox.ac.uk

ORCiD: 0000-0002-9562-3520

T. Woollings

Atmospheric, Oceanic and Planetary Physics, University of Oxford, Parks Road, Oxford OX1 3PU, UK

ORCiD: 0000-0002-5815-9079

C. Mbengue

Atmospheric, Oceanic and Planetary Physics, University of Oxford, Parks Road, Oxford OX1 3PU, UK

ORCiD: 0000-0001-6378-7419

M. R. Allen

Atmospheric, Oceanic and Planetary Physics, University of Oxford, Parks Road, Oxford OX1 3PU, UK

Environmental Change Institute, School of Geography and the Environment, University of Oxford, South  
Parks Road, Oxford OX1 3QY, UK

C. H. O'Reilly

Atmospheric, Oceanic and Planetary Physics, University of Oxford, Parks Road, Oxford OX1 3PU, UK

ORCiD: 0000-0002-8630-1650

7 **Abstract** We investigate the opposing effects of direct radiative forcing and sea surface  
8 warming on the atmospheric circulation using a hierarchy of models. In three general cir-  
9 culation models, direct CO<sub>2</sub> forcing produces a wavenumber 5 stationary wave over the  
10 Northern Hemisphere in summer. Sea surface warming produces a similar wave, but with  
11 the opposite sign. The waves are also present in the Coupled Model Intercomparison Project  
12 phase 5 ensemble with opposite signs due to direct CO<sub>2</sub> and sea surface warming. Analy-  
13 ses of tropical precipitation changes and equivalent potential temperature changes and the  
14 results from a simple barotropic model show that the wave is forced from the tropics. Key  
15 forcing locations are the Western Atlantic, Eastern Atlantic and in the Indian Ocean just off  
16 the east coast of Africa. The stationary wave has a significant impact on regional temper-  
17 ature anomalies in the Northern Hemisphere summer, explaining some of the direct effect  
18 that CO<sub>2</sub> concentration has on temperature extremes. Ultimately, the climate sensitivity and  
19 future changes in the land-sea temperature contrast will dictate the balance between the op-  
20 posing effects on regional changes in mean and extreme temperature and precipitation under  
21 climate change.

22 **Keywords** Stationary waves · Radiative forcing · Sea surface warming · Midlatitude  
23 circulation · Land-sea thermal contrast · Rossby waves

---

H. Shiogama

Center for Global Environmental Research, National Institute for Environmental Studies, Tsukuba, Japan

ORCID: 0000-0001-5476-2148

S. Sparrow

Oxford e-Research Centre, Department of Engineering Science, University of Oxford, Parks Road, Oxford  
OX1 3PJ, UK

ORCID: 0000-0002-1802-6909

<sup>24</sup> **1 Introduction**

<sup>25</sup> It is well established that there are differing, and sometimes opposing, effects of radiative  
<sup>26</sup> forcing versus sea surface temperature (SST) change on the atmospheric circulation (e.g.  
<sup>27</sup> Mitchell 1983; He and Soden 2015; Shaw and Voigt 2015; Chadwick et al. 2017). Land  
<sup>28</sup> warming is primarily driven by the SST warming of the oceans, an indirect effect of anthro-  
<sup>29</sup> pogenic emissions, rather than the direct response to increasing greenhouse gases (GHGs)  
<sup>30</sup> over land (Compo and Sardeshmukh 2009). However, global mean temperature increase  
<sup>31</sup> driven by the SST warming is not the sole driver of changes in temperature and precipita-  
<sup>32</sup> tion patterns (Folland et al. 1998; Sexton et al. 2003; Bony et al. 2013; Dong and Sutton  
<sup>33</sup> 2015; Richardson et al. 2016) or extremes (Kamae et al. 2014a; Seneviratne et al. 2014;  
<sup>34</sup> Dong et al. 2016; Baker et al. 2018a).

<sup>35</sup> Shaw and Voigt (2015) investigate the large scale circulation responses to direct CO<sub>2</sub>  
<sup>36</sup> radiative forcing versus SST warming in the Coupled Model Intercomparison Project phase  
<sup>37</sup> 5 (CMIP5) ensemble, finding that CO<sub>2</sub> forcing leads to positive land-sea equivalent po-  
<sup>38</sup> tential temperature ( $\theta_e$ ) contrasts, and SST forcing leads to negative land-sea  $\theta_e$  contrasts.  
<sup>39</sup> In the CO<sub>2</sub> case, the positive land-sea  $\theta_e$  contrasts lead to low-level convergence around  
<sup>40</sup> Asia, a stronger Asian monsoon cyclone and Pacific anticyclone, and a poleward shift of  
<sup>41</sup> the Pacific jet stream. The negative land-sea  $\theta_e$  contrasts in the SST case lead to the oppo-  
<sup>42</sup> site effects on the circulation. However, Shaw and Voigt (2015) do not look specifically at  
<sup>43</sup> changes in midlatitude stationary waves in response to the two types of forcing, which may  
<sup>44</sup> have an important impact on future changes in regional Northern Hemisphere (NH) summer  
<sup>45</sup> temperatures and heatwave hazard due to the direct effect of CO<sub>2</sub> shown by Baker et al.  
<sup>46</sup> (2018a).

47 A key factor in the opposing circulation responses comes from the differing land-sea  
48 contrast response to radiative forcing versus SST warming (Kamae et al. 2014b; Shaw and  
49 Voigt 2015). The land-sea contrast arises from the non-linearity of the Clausius-Clapeyron  
50 relationship of saturation specific humidity to temperature (Joshi et al. 2008). The dynamical  
51 precipitation response to direct CO<sub>2</sub> forcing has been associated with the land-sea contrast,  
52 leading to an increase in precipitation over tropical land, and a decrease over the oceans  
53 due to a weakening of the overturning circulation (Bony et al. 2013). Upper tropospheric  
54 heating stabilises the atmosphere which leads to a decrease in convection (He and Soden  
55 2015). However, in response to the heating the land warms and destabilises the atmosphere,  
56 leading to an increase in convection over land (Bony et al. 2013).

57 Changes in convection can cause changes in the upper-level divergence, which can force  
58 Rossby waves that can propagate from the tropics into the extratropics (Sardeshmukh and  
59 Hoskins 1988). Specifically, changes in the Walker circulation have been shown to affect  
60 upper tropospheric divergence and produce a stationary wave with wavenumber 5 over the  
61 NH midlatitudes in winter (Haarsma and Selten 2012) which strongly resembles the circum-  
62 global wave guide pattern described by Branstator (2002). The NH summer circulation also  
63 has a wave 5 circumglobal wavetrain associated with natural variability (Ding and Wang  
64 2005), which has a forced component arising from the tropics (Ding and Wang 2007; Yasui  
65 and Watanabe 2010).

66 Schubert et al. (2011) suggest that stationary Rossby waves can play an important role  
67 in causing NH summer heat extremes and Screen and Simmonds (2014) show the link be-  
68 tween extreme weather event frequency in the NH and amplified stationary planetary waves.  
69 Studies using reanalysis (Cassou et al. 2005) and model data (Lee et al. 2017) point towards  
70 tropical forcing in exciting Rossby waves that cause extremes. One particular theory of how  
71 summer stationary waves cause heat extremes is quasiresonant amplification (Petoukhov

et al. 2013). However, in this study we show that simple changes in tropical forcing can trigger stationary Rossby waves that can affect heat extremes. Previous studies identify the tropical Atlantic (Cassou et al. 2005), tropical Pacific and Caribbean (Wulff et al. 2017), Indian monsoon region (Joseph and Srinivasan 1999; Lin 2009) and equatorial Africa (Yasui and Watanabe 2010) as important Rossby wave forcing regions. We aim to diagnose the important forcing locations for the stationary waves seen in response to the SST and CO<sub>2</sub> forcings.

Here we investigate the responses of precipitation and NH stationary waves in response to these two types of forcings. We use three general circulation models (GCMs) and the CMIP5 ensemble to show that both SST warming and direct CO<sub>2</sub> forcing produce a summer stationary wave over the NH midlatitudes, but that the two forced waves are in antiphase. We develop and test a theory on the midlatitude circulation response to SST warming and direct CO<sub>2</sub> forcing. We show that the two different forcings produce opposite changes in divergence (and corresponding opposite changes in precipitation) in the tropics, leading to waves in antiphase. These opposite divergence responses arise from the opposite responses of land-sea  $\theta_e$  contrasts and the differing thermodynamic effects of radiative forcing versus SST increase. We then test our hypothesis that the anomalous forcings produce the stationary wave using a simple barotropic model to reproduce the GCM wave response and identify key forcing locations.

Section 2 outlines the methods and models used in the study. Section 3 presents the GCM results leading us to perform the barotropic model experiments which we analyse in Section 4. Section 5 discusses the relevance of the work and the implications of our findings, before the final conclusions in Section 6.

---

**95 2 Methods****96 2.1 GCM data**

97 In this study, we use results from three general circulation models (GCMs): HadAM3P,  
98 MIROC5 (Watanabe et al. 2010) and CAM4 (Gent et al. 2011). HadAM3P is an atmosphere  
99 only, medium resolution, GCM developed by the UK Met Office. It is based upon the atmo-  
100 spheric component of HadCM3 (Pope et al. 2000; Gordon et al. 2000). We use an improved  
101 version of HadAM3P which has a more sophisticated land-surface scheme (Guillod et al.  
102 2017). We run HadAM3P using the large-ensemble capability provided by the climatepre-  
103 diction.net volunteer computing network (Allen 1999; Guillod et al. 2017), where members  
104 of the public run initial condition ensemble GCM simulations. We compare results from  
105 HadAM3P (run at  $1.25^\circ \times 1.875^\circ$  resolution) to MIROC5 and CAM4 (run at  $1.4^\circ \times 1.4^\circ$  and  
106  $1.9^\circ \times 2.5^\circ$  resolutions respectively). The models are run as Atmospheric Model Intercom-  
107 parison Project (AMIP) style ensembles (Taylor et al. 2012) with prescribed SSTs and sea  
108 ice. All the ensembles and their setups are summarised in Table 1.

**109 2.1.1  $1.5^\circ\text{C}$  experiments**

110 The first set of experiments, the  $1.5^\circ\text{C}$  experiments, have two ensembles for each model,  
111 which use the Half a degree Additional warming, Prognosis and Projected Impacts (HAPPI;  
112 [www.happimip.org](http://www.happimip.org)) design (Mitchell et al. 2017). These two ensembles use SSTs and bound-  
113 ary conditions to simulate conditions in a world  $1.5^\circ\text{C}$  warmer than pre-industrial (1861-  
114 1880) conditions. Here we use the HAPPI Tier 1 experimental design (Mitchell et al. 2017),  
115 which uses the multi-model mean SST patterns; thus, all ensembles and models are run with  
116 an identical time varying  $1.5^\circ\text{C}$  SST pattern. The full details are discussed in Mitchell et al.  
117 (2017).

118 The two ensembles differ only in CO<sub>2</sub> concentration, but otherwise use the RCP2.6 sce-  
119 nario forcings from the last decade of the 21st century. In HadAM3P and MIROC5, CO<sub>2</sub> is  
120 fixed at 395.8ppm (hereafter the LCO<sub>2</sub> ensemble) and 550.0ppm (HCO<sub>2</sub> ensemble), repre-  
121 senting the lower and higher likely CO<sub>2</sub> concentrations averaged over 2091-2100 in adaptive  
122 pathways that succeed in achieving warming below 1.5°C in 2100 for the assessed ranges  
123 of climate response uncertainty (Millar et al. 2017). For CAM4, we use experiments with  
124 the CO<sub>2</sub> fixed at 379.0ppm and 423.1ppm; hence, differences between the CAM4 ensem-  
125 bles still occur due to the difference in CO<sub>2</sub> concentration, but should not be quantitatively  
126 compared to the other two models. All CO<sub>2</sub> concentrations are prescribed as a global mean  
127 atmospheric concentration and the CO<sub>2</sub> is well-mixed. All ensemble members are run for 11  
128 years, with the first year discarded to allow the atmosphere to spin up. For HadAM3P there  
129 are 98 and 119 members for the LCO<sub>2</sub> and HCO<sub>2</sub> ensembles respectively. Both MIROC5  
130 ensembles have 50 members, and both CAM4 ensembles have 501 members. For the full  
131 details of these ensembles, see Baker et al. (2018a).

132 *2.1.2 Hadley experiments*

133 We run a further three ensembles just using HadAM3P, the Hadley experiments. These en-  
134 sembles, named NAT, GHG and SST, are designed to isolate the response of the atmosphere  
135 to SST forcings and GHG forcings associated with global warming separately. The NAT en-  
136 semble has natural SSTs and GHGs which simulates a world with no anthropogenic climate  
137 change. The NAT SSTs are calculated by removing the modelled anthropogenic warming  
138 from observed SSTs. The anthropogenic warming is calculated as in Haustein et al. (2016):  
139 11 GCM simulations from the CMIP5 archive are averaged and the monthly climatologies  
140 (1996-2005) of the *HistoricalNat* simulations are subtracted from the *Historical* simula-  
141 tions. The mean of these 11 patterns is used as the SST pattern for the NAT ensemble and

142 pre-industrial atmospheric GHG concentrations (IPCC 1900 forcing) are used to force the  
 143 NAT ensemble. For further details, see Haustein et al. (2016) and Schaller et al. (2016).  
 144 The GHG ensemble uses the NAT SSTs, with RCP4.5 GHGs (from 2005-2015). The SST  
 145 ensemble uses the observed 2005-2015 SSTs from the OSTIA SST dataset (Donlon et al.  
 146 2012) and pre-industrial GHGs. The CO<sub>2</sub> concentration of the NAT and SST ensembles  
 147 is 284.4ppm, the average CO<sub>2</sub> concentration of the GHG ensemble is 390.4ppm. Sea ice  
 148 for the NAT and GHG ensembles is taken from the maximum well-observed sea ice (DJF  
 149 1986/1987), for the SST ensemble the 2005-2015 observed OSTIA sea ice is used. Volcanic  
 150 forcings are set to zero in all three ensembles, and the solar forcing is taken from 2005-2015.  
 151 All three ensembles are run for 11 years, with the first year discarded. There are 124, 118  
 152 and 113 ensemble members for the NAT, GHG and SST ensembles respectively.

153 *2.1.3 CMIP5 experiments*

154 We also make use of AMIP data from the AMIP control, AMIP4K and AMIP4xCO<sub>2</sub> sim-  
 155 ulations (Taylor et al. 2012) from the following CMIP5 models: bcc-csm1-1, CanAM4,  
 156 CNRM-CM5, FGOALS-g2, HadGEM2-A, IPSL-CM5A-LR, IPSL-CM5B-LR, MPI-ESM-  
 157 LR and MPI-ESM-MR. All simulations are forced with historical SSTs and greenhouse  
 158 gases and are run over the 30-year period 1979-2008.

159 *2.2 Barotropic model*

160 In this study we employ the idealised barotropic model from O'Reilly et al. (2018). Follow-  
 161 ing Hoskins and Ambrizzi (1993), the model integrates the barotropic vorticity equation on  
 162 a sphere:

$$\left( \frac{\partial}{\partial t} + \mathbf{u}\psi \cdot \nabla \right) \zeta = F - \lambda \zeta - \mu \nabla^4 \zeta, \quad (1)$$

163 where  $\mathbf{u}_\Psi$  is the rotational velocity field,  $\zeta$  is the absolute vorticity (the sum of planetary and  
 164 relative vorticity components),  $F$  is a constant forcing term,  $\lambda$  is a linear damping rate with  
 165 a timescale of 10 days, and  $\mu = 2.4 \times 10^{16} \text{ m}^4 \text{ s}^{-1}$  is a biharmonic diffusion coefficient. The  
 166 equation is solved using spectral harmonics with a triangular truncation at wavenumber 42  
 167 (i.e. T42). The forcing is decomposed into two terms,  $F = \bar{F} + F'$ , where  $\bar{F}$  is selected to  
 168 maintain the basic state exactly, which is taken to be the climatological vorticity field at 200  
 169 hPa from the relevant dataset.

170 The model output from HadAM3P, used as the background state in the barotropic model,  
 171 includes winds on 850, 500 and 200 hPa pressure surfaces. We choose the 200 hPa winds to  
 172 calculate the climatological vorticity field for the barotropic model; the anomalous tropical  
 173 forcing (via divergent outflow) is strongest in the upper troposphere (e.g. Krishnamurti et al.  
 174 2013); and vorticity gradients, upon which the signal propagates out of the tropics, are also  
 175 significantly stronger in the upper troposphere. It is necessary that the basic state includes  
 176 these strong wave guides to achieve a reasonable response, both in amplitude and pattern  
 177 (O'Reilly et al. 2018).

178 The anomalous forcing  $F'$ , is selected to mimic the forcing of the barotropic vorticity  
 179 equation by divergent outflow in the tropics. Following Sardeshmukh and Hoskins (1988),  
 180 the linearised Rossby wave source (RWS) anomaly  $S'$  is given by

$$S' = -\mathbf{u}'_\chi \cdot \nabla \bar{\zeta} - \bar{\mathbf{u}}_\chi \cdot \nabla \zeta' - \bar{\zeta} D' - \zeta' \bar{D}, \quad (2)$$

181 where  $\mathbf{u}_\chi$  is the divergent velocity field and  $D = \nabla \cdot \mathbf{u}_\chi$  is the divergence. Here the over  
 182 bars and the primes denote climatological and anomaly fields respectively. In this study, we  
 183 force the model with a RWS anomaly due only to anomalous divergence and anomalous  
 184 transports of mean vorticity. We ignore terms due to anomalous vorticity, as these terms  
 185 largely correspond to the circulation response we are assessing. The forcing term therefore

<sup>186</sup> reduces to:

$$S' = -\mathbf{u}' \cdot \nabla \bar{\zeta} - \bar{\zeta} D' = F'. \quad (3)$$

<sup>187</sup> The model is initialised from the basic state and integrated forward for 25 days. The re-  
<sup>188</sup> sponse becomes quasi-stationary after about two weeks, so the stationary response to forcing  
<sup>189</sup> is presented as the average over the period 16-20 days.

### <sup>190</sup> 3 GCM results

<sup>191</sup> The June-July-August (JJA) difference in precipitation (colours) and 200 hPa meridional  
<sup>192</sup> wind (contours) between ensemble mean HCO<sub>2</sub> and LCO<sub>2</sub> (CO<sub>2</sub> response) ensembles are  
<sup>193</sup> shown in Fig. 1. The pattern of tropical precipitation change in the CO<sub>2</sub> response for the  
<sup>194</sup> three models is very similar: a wetting over land and a drying over the oceans. This is  
<sup>195</sup> associated with a poleward shift of the intertropical convergence zone (ITCZ) over the Sahel  
<sup>196</sup> region of Western Africa.

<sup>197</sup> We also observe a circumglobal wave pattern over the NH between 30°N-70°N. Whilst  
<sup>198</sup> the strength of the wave varies spatially in the different models, a wavenumber 5 stationary  
<sup>199</sup> wave with wave centres in the same locations is observed in all three CO<sub>2</sub> responses. Due to  
<sup>200</sup> large ensemble sizes and long runs, the responses of the tropical precipitation and meridional  
<sup>201</sup> wind are both statistically significant (not shown).

<sup>202</sup> Very similar stationary wave and precipitation responses to CO<sub>2</sub> forcing are evident and  
<sup>203</sup> robust in the difference between the multi-model-mean of the AMIP4xCO<sub>2</sub> and AMIP con-  
<sup>204</sup> trol (AMIP4xCO<sub>2</sub> response) ensembles (Fig. 2a, individual model responses in Fig. S1). The  
<sup>205</sup> responses to a uniform SST increase are shown in Fig. 2b (individual model responses in Fig.  
<sup>206</sup> S2), the difference between the multi-model mean AMIP4K and AMIP control (AMIP4K  
<sup>207</sup> response) ensembles. Here, there is an opposite response in the precipitation over the tropical

208    Atlantic and over the tropical region of Africa compared to the response to CO<sub>2</sub>. The station-  
209    ary wave is still present, but with the wave centres in antiphase to the CO<sub>2</sub> and AMIP4xCO<sub>2</sub>  
210    responses.

211    A similar picture emerges when we consider the difference between the GHG and NAT  
212    (GHG response) ensembles, and SST and NAT (SST response) ensembles (Figs. 2c,d). The  
213    GHG response shows increased precipitation over the tropical region of Africa, and de-  
214    creased precipitation over the tropical Atlantic. The stationary wave is present, with the  
215    same wave centres as the CO<sub>2</sub> and AMIP4xCO<sub>2</sub> responses. In agreement with the AMIP4K  
216    response, the SST response is almost diametrically opposed to the CO<sub>2</sub> and AMIP4xCO<sub>2</sub>  
217    responses: drying over the tropical regions of Africa and wetting over the tropical Atlantic.  
218    The stationary wave is also apparent in the SST response with the same wave centre loca-  
219    tions as the AMIP4K response.

220    To summarise the precipitation and meridional wind changes, we plot the differences  
221    between the AMIP4xCO<sub>2</sub> and AMIP4K responses and the differences between the GHG  
222    and SST responses in Fig. 3. This emphasises the important features consistent between the  
223    responses to direct CO<sub>2</sub> forcing and SST warming, and removes elements of noise. It is  
224    clear that the consistent precipitation changes between the CMIP5 experiments and Hadley  
225    experiments are located in the tropics over the Atlantic, Africa and Central-West Pacific.  
226    The wave 5 pattern and wave centres in the two experiments are also co-located, with slight  
227    differences over Europe.

228    Before examining the origin of the stationary wave, we investigate what impact such a  
229    wave has on NH temperature. As shown by Baker et al. (2018a), the ensemble mean JJA  
230    temperature response in the CO<sub>2</sub> forced ensembles is a wavelike positive-negative temper-  
231    ature anomaly pattern across the NH in JJA, which is associated with increases in extreme  
232    temperature events. We focus on the 1.5°C and Hadley experiment results as we have large

233 ensembles for these models, as opposed to the one realization from each model in the CMIP5  
234 AMIP ensemble. We use a simple linear regression to diagnose the relationship between the  
235 temperature anomalies and the stationary wave.

236 We first define the response of a particular member as the difference between the HCO<sub>2</sub>  
237 ensemble member 10-year mean and the LCO<sub>2</sub> ensemble mean across the ensemble mem-  
238 bers. For each member we create a circulation index by subjectively taking the locations of  
239 the maximum clearly defined wave centres in the JJA ensemble mean 200 hPa meridional  
240 wind responses (see dots in Fig. 4 for wave centre locations). We sum the positive wave  
241 centres (pink dots) and subtract the negative wave centres (green dots) to give a circulation  
242 index for each ensemble member response. We then regress the standardized circulation in-  
243 dices for each ensemble member against the ensemble member mean temperature response  
244 at each gridpoint.

245 The regression coefficients are plotted in Fig. 4. They show that members with a strong  
246 circulation index response have strong temperature anomalies compared to members with  
247 weaker circulation index responses. Regions where the stationary wave is anticyclonic are  
248 associated with regions of increased temperature, and cyclonic regions are associated with  
249 regions of decreased temperature. Anticyclonic regions are typically characterised by clear  
250 skies, which leads to greater incident solar radiation on the Earth's surface, hence an in-  
251 crease in surface temperature (Bieli et al. 2015). The temperature anomalies are completely  
252 opposite for the SST case, which supports the link between the wave and the temperature  
253 anomalies further. In the CO<sub>2</sub> cases, the regions of positive temperature anomaly are co-  
254 located with the NH regions that see increases in heat extremes under higher CO<sub>2</sub> concen-  
255 trations in Baker et al. (2018a). This suggests that the direct circulation response to higher  
256 CO<sub>2</sub> concentrations governs the regional differences in increases in extremes. It is worth  
257 noting that this regression approach likely underestimates the effect of the circulation on

temperature as the circulation index is comprised of wave centres across the NH. As we will show in Section 4, the wave is actually forced from several different locations which contribute to parts of the wavetrain meaning the full wave is not necessarily present all the time in each ensemble member. This suggests that if a single wave centre were used as the circulation index, there would be a larger local regression coefficient and therefore a larger effect on the local temperature.

A potential mechanism for the emergence of a stationary wave response to forcing is through changes in convection in the tropics forcing a Rossby wave that then propagates into the midlatitudes (Haarsma and Selten 2012). These changes in convection can cause changes in upper-level divergence (with associated precipitation changes) which can be captured by changes in the RWS. One robust precipitation change is the decrease in precipitation in the tropical Western Atlantic and Caribbean Sea for the CO<sub>2</sub> forced cases (Fig. 1 and Figs. 2a,c), and an increase in the SST forced cases (Figs. 2b,d). A second robust change is the increase in precipitation in the tropical regions of Africa for the CO<sub>2</sub> forced cases (Fig. 1 and Figs. 2a,c), and a decrease in the SST forced cases (Figs. 2b,d). The reasons behind these observed changes will be explored in Section 5, for now we just seek to highlight these regions as potentially important regions where changes in the divergence lead to changes in the RWS. We choose to investigate the wave response further in HadAM3P given the data available from the Hadley experiments for both GHG and SST forcing cases plus the fact that HadAM3P exhibits the clearest wave response (see Fig. 1).

#### 278 **4 Barotropic model results**

279 To further investigate the possibility of the wave being forced in the tropics, we perform a  
280 series of experiments with the barotropic model. As outlined in Section 2.2, we compute the

281 RWS (neglecting anomalous vorticity terms). We do this using the NAT ensemble mean as  
282 the 200hPa climatological fields (overbar variables in equation 3) and define the anomalous  
283 fields (primed variables) as the GHG (or SST) ensemble minus the NAT ensemble 200  
284 hPa fields. To test whether the barotropic model responses are linear, we multiply the input  
285 forcings by  $10^{-6}$  (and then scale the output fields back up by  $10^6$ ). Sensitivity experiments  
286 with and without the linearisation applied display no differences, and so the remainder of the  
287 barotropic experiments use the unscaled forcings. To first test that the barotropic model can  
288 produce the stationary wavelike response in the full GCMs, we force the barotropic model  
289 using the anomalous May RWS forcings from the GHG and SST ensembles, with the June  
290 NAT vorticity background state. The May forcing and June background state are chosen as  
291 sensitivity tests using different background state months and anomalous forcing months (not  
292 shown) show this combination gives the biggest and clearest Rossby wave response.

293 The results of these two experiments are shown in Fig. 5. Anomalous forcing is only  
294 applied between  $0^\circ$ - $10^\circ\text{N}$  (pink box in Figs. 5a,b). The forcings in the GHG and SST cases  
295 are opposite in several regions including the Western Atlantic, Eastern Atlantic and in the  
296 Indian Ocean, just off the east coast of Africa. Anomalous RWS forcings arise from changes  
297 in tropical convective heating (Sardeshmukh and Hoskins 1988), caused by the changes in  
298 precipitation in the tropics. The co-location of precipitation responses and anomalous RWS  
299 forcings suggest that the precipitation changes are responsible for the anomalous RWS forc-  
300 ings. A comparison between the barotropic meridional wind responses (Figs. 5c,d) and the  
301 full model responses (Figs. 2c,d) reveals that the barotropic model can capture the main fea-  
302 tures of the full model. The wave pattern is clearly visible in both GHG and SST barotropic  
303 model experiments, with the same wavenumber as in the full model responses. Wave cen-  
304 tres in the barotropic cases are shifted slightly eastward compared to the wave in the JJA  
305 mean in the Hadley experiments. However, the June mean wave centres in the Hadley ex-

306 experiments are also shifted by a similar amount eastward from the JJA mean (not shown),  
307 indicating that the shift between the wave in the barotropic model and the Hadley exper-  
308 iments could be due to the background winds differing between June and the JJA mean.  
309 Some wave centres are not as far poleward as in the full model response. This is evident  
310 in the jet exit regions, where climatological vorticity gradients are weak (e.g. over Northern  
311 Europe); there, a simple barotropic model will struggle to propagate the wave. Other reasons  
312 for the wave differences include the barotropic model not capturing important feedbacks that  
313 occur in the full model, such as zonal wind changes, eddy mean flow interactions, or poten-  
314 tially important non-linear orographic interactions (Ting 1994). Nevertheless, the fact that  
315 the barotropic model results bear strong similarity to the full model is remarkable given the  
316 model's simplicity.

317 Fig. 3c summarises the forcing used and the wave response in the barotropic model,  
318 taking the difference between GHG and SST RWS forcings and barotropic model merid-  
319 ional wind responses to highlight the areas of consistent change between the two ensem-  
320 ble responses. The strongest RWS signal is in the Indian Ocean; there is a dipole in the  
321 tropical Atlantic and various consistent regions across the Pacific too. The stationary wave  
322 responses in the barotropic model are very similar to the GCM responses, suggesting the  
323 GCM responses are indeed forced from the tropics.

324 To test whether the observed wave is a new forced wave, or an excitation of a wave  
325 in the climatological background state, we perform the same experiments after removing  
326 wavenumbers 4-6 from the background state. The barotropic model responses in this case  
327 still display the same wave pattern with wavenumber five (not shown), implying that the  
328 wave is a new forced wave due to the anomalous RWS. These results show that the stationary  
329 wave arises from anomalous wave forcing, not from changes in the zonal winds.

330 To determine the forcing locations responsible for producing the wave response in the  
 331 barotropic model, we perform a set of sensitivity experiments using the barotropic model.  
 332 Following Barsugli and Sardeshmukh (2002), we apply a series of 64 cosine-square patch  
 333 forcings of the form:

$$F'_j(\lambda, \phi) = A \cos^2\left(\frac{\pi}{2} \frac{\phi - \phi_i}{\phi_w}\right) \cos^2\left(\frac{\pi}{2} \frac{\lambda - \lambda_j}{\lambda_w}\right) \quad (4)$$

334 on the rectangle  $\phi_i \pm \phi_w, \lambda_j \pm \lambda_w$  (where  $\phi$  is the latitude and  $\lambda$  is the longitude), and zero  
 335 elsewhere. The half-widths of the patches are fixed at two gridpoints in both the latitudinal  
 336 and longitudinal directions, yielding  $\phi_w \approx 5.58^\circ$  and  $\lambda_w = 5.625^\circ$ . We apply the patch cen-  
 337 tres at a single fixed latitude  $\phi_i = 7.0^\circ$ , whilst increasing  $\lambda$  in  $5.625^\circ$  increments starting at  
 338  $0^\circ$ , giving 64 patches in total for each sensitivity experiment. The amplitude of the patches,  
 339  $A = 2.5 \times 10^{-11} \text{ s}^{-2}$ , is chosen to be on the order of magnitude of, but slightly larger than,  
 340 the forcing observed in the GHG forced ensemble so as to produce a strong signal in the  
 341 barotropic model.

342 To assess the importance of a particular patch location in forcing the HadAM3P merid-  
 343 ional wind response, we assign the following weight to each patch experiment response:

$$w_j = \frac{v_j^b \cdot \bar{v}}{\bar{v} \cdot \bar{v}}, \quad (5)$$

344 where  $v_j^b$  is the meridional wind response averaged between days 16-20 in the barotropic  
 345 model for forcing  $F'_j$ , and  $\bar{v}$  is the June ensemble mean meridional wind response from the  
 346 HadAM3P model. The dot products are computed using cosine latitude weighting, and over  
 347 the region  $30^\circ\text{N}-70^\circ\text{N}$  and all longitudes.

348 We perform two sets of sensitivity experiments, one using the HadAM3P NAT ensem-  
 349 ble mean June background state, and the other using the NCEP Reanalysis 2 1979-2015  
 350 June mean background state (NCEP Reanalysis 2 data provided by the NOAA/OAR/ESRL

351 PSD, Boulder, Colorado, from their website at <http://www.esrl.noaa.gov/psd/>). We then cal-  
352 culate a set of weights (comprising of 64 weights, one for each patch position) for each of  
353 the following four cases: the meridional wind responses of the barotropic model using the  
354 NAT ensemble mean background state projected onto the GHG ensemble mean meridional  
355 wind response, NAT background onto SST ensemble wind response, NCEP background  
356 onto GHG ensemble wind response and NCEP background onto SST ensemble wind re-  
357 sponse.

358 We calculate the weights for the sensitivity experiment responses with the full model  
359 GHG (Fig. 6a) and SST (Fig. 6b) responses in the 200 hPa meridional wind. Weights are  
360 shown for NAT background (blue). The RWS forcings from the full model (used to force  
361 the barotropic model in Fig. 5) averaged over  $0^{\circ}$ - $10^{\circ}$ N are shown in red. Red lines are  
362 normalised so the maximum in each figure is the same as the respective blue line showing  
363 the NAT weights. Lines in Fig. 6b have been multiplied by -1 to allow direct comparison  
364 with Fig. 6a. Regions where the amplitude of the full model forcing and weights agree and  
365 are large indicate regions where forcing is likely to be important in producing the full model  
366 wave responses. From the weights, we identify three key regions: the Western Atlantic,  
367 Eastern Atlantic and in the Indian Ocean, just off the east coast of Africa (marked by the  
368 crosses in Figs. 6c,d,e). For the SST case, there also seems to be a region of importance in  
369 the Pacific. Here we focus on the other three regions as they appear important in both GHG  
370 and SST cases. Figs. 6c,d,e show the wave responses for the HadAM3P background case at  
371 each of the identified forcing locations. The forcing in the Eastern Atlantic has a negative  
372 weight, and so we multiply the response of this patch experiment by -1 to give the correct  
373 meridional wind response. When the three forcings are combined (Fig. 6f), they reproduce  
374 the wave response that the full model forcing produces in the barotropic model (compare  
375 to Fig. 5c). We combine the responses by summing them linearly to produce the response

376 in Fig. 6f, but we verify that applying the three forcings in the same run produces the same  
377 wave response (not shown) indicating that the forcings combine linearly.

378 To test the robustness of the response to the identified forcing locations and jet condi-  
379 tions, we analyse the sensitivity results from the experiments run with the NCEP background  
380 state. The green lines in Figs. 6a,b show the weights when using the NCEP background  
381 state. The NCEP weights are broadly consistent with the NAT weights, albeit with a weaker  
382 sensitivity to the Indian Ocean region. When forced at the same three identified locations  
383 (marked by the crosses) the combined wave response is broadly the same as when using  
384 the NAT background state (Fig. 6g), with differences mainly arising over jet exit regions for  
385 the reasons previously discussed regarding weaker climatological vorticity gradients. From  
386 these sensitivity experiments we can conclude that there exist three important forcing loca-  
387 tions to produce the full model wave response, and that the wave response also occurs on an  
388 observed background state (the NCEP case), which implies that the wave responses are not  
389 just possible in the three GCMs, but also in reality.

390 The replication of the wave 5 in the barotropic model is only possible using the June  
391 background state from HadAM3P (in both the Hadley experiments and 1.5°C experiments)  
392 and from reanalysis. We tried different months and also using the CAM4 and MIROC5 200  
393 hPa vorticity fields as the background state. In all other cases besides the June reanalysis and  
394 HadAM3P cases, a forced wave is present, but as a wave 4 pattern and not as a circumglobal  
395 wave. To investigate this we look at the jet biases in the three different models. A different  
396 background state with different midlatitude zonal wind could affect the waveguiding prop-  
397 erties of the jet due to the dependence of Rossby wave phase speed on jet speed (Ambrizzi  
398 et al. 1995). This has been shown to cause changes in winter stationary waves in GCMs  
399 (Simpson et al. 2016).

400 If the differences between the midlatitude zonal wind in the background states is the  
401 reason why we can reproduce the wave in only specific conditions, we might expect the  
402 HadAM3P midlatitude jet to be more equatorward than the other two models. A further  
403 equatorward jet would mean that the waveguide is closer to potential wave forcings in the  
404 tropics. This proximity to the tropics would indicate a stronger wavetrain, as seen in the  
405 HadAM3P full model response, as anomalous divergent winds in the tropics are closer to  
406 the vorticity gradients in the midlatitudes required for the wave to propagate. Biases in the  
407 jet speed could affect the wavenumber of the wave due to the dependence of Rossby wave  
408 phase speed on jet speed. Fig. 7 shows the 200 hPa June ensemble mean zonal wind biases of  
409 the three models compared to the 1979-2015 200 hPa June mean zonal wind from the NCEP  
410 2 Reanalysis . The Pacific jet in both CAM4 and MIROC5 exhibits poleward biases, whilst  
411 in HadAM3P, the jet has a weak bias. All three model jets exhibit a poleward biased jet over  
412 land. Over the Atlantic, the biases in HadAM3P are again the smallest, with only a slightly  
413 weak biased jet compared to strong biased jets in the other two models. The HadAM3P jet is  
414 narrower in the zonal mean than the MIROC5 and CAM4 jets, and it has been suggested that  
415 this increases the ability of a jet to act as a waveguide (Manola et al. 2013). The narrowness  
416 and lack of a poleward bias in HadAM3P may suggest why using it as the background state  
417 for the barotropic model can give the wave 5 pattern whereas the other models cannot.

## 418 5 Discussion

419 We identify two classes of mechanism which cause the changes in tropical precipitation in  
420 response to the CO<sub>2</sub> and SST forcings. The first of these is due to thermodynamic changes.  
421 Increases in atmospheric CO<sub>2</sub> concentration lead to an increase in the static stability of the  
422 atmosphere due to enhanced longwave absorption by the extra CO<sub>2</sub>, thus suppressing con-

423 vention (Sugi and Yoshimura 2004; Andrews et al. 2009; Dong et al. 2009; Cao et al. 2012;  
424 Bony et al. 2013). On the other hand, an increase in SSTs results in increased atmospheric  
425 moisture, leading to an increase in precipitation across tropical wet regions (Held and So-  
426 den 2006; Seager et al. 2010). These thermodynamic effects are responsible for the model  
427 changes in precipitation over the tropical Western Atlantic. In the CO<sub>2</sub> forcing cases, the  
428 suppressed convection leads to a decrease in precipitation in the tropical Western Atlantic  
429 (Fig. 1 and Figs. 2a,c). In the SST forcing cases, the enhanced moisture leads to an increase  
430 in the precipitation in the tropical Western Atlantic (Figs. 2b,d).

431 The second mechanism arises from the land-sea  $\theta_e$  contrast. Increases in CO<sub>2</sub> cause the  
432 land to warm in response to increased downwelling longwave radiation, enhancing the land-  
433 sea  $\theta_e$  contrast (Shaw and Voigt 2015) and leading to increases in precipitation over land  
434 (Chadwick et al. 2014; Richardson et al. 2016). However, when the SSTs are increased, the  
435 land-sea  $\theta_e$  contrast changes in the opposite direction (Shaw and Voigt 2015), causing an  
436 increase in the vertical velocity over the oceans (likely due to a reduction in static stability)  
437 thus enhancing convective precipitation over the oceans (Chadwick 2016). The changes in  
438 the land-sea  $\theta_e$  contrast in the GHG and SST responses are shown in Fig. 8. In the GHG  
439 case (Fig. 8a) on the east coast of Africa, there is a positive land-sea  $\theta_e$  gradient (along the  
440 blue arrow in Fig. 8a) and associated increase in precipitation over the same region in the  
441 CO<sub>2</sub> forcing cases (Fig. 1 and Figs. 2a,c). On the west coast Sahel region of Africa however,  
442 there is a negative land-sea  $\theta_e$  gradient (black arrow) which is associated with a decrease in  
443 precipitation. The changes in  $\theta_e$  correspond to the RWS forcing in the two regions: positive  
444 RWS for a positive land-sea  $\theta_e$  contrast and negative RWS for a negative contrast (see Fig.  
445 5a). These regions of positive and negative RWS forcing are consistent with the Eastern  
446 Atlantic weight being opposite in sign to the Western Atlantic and Indian Ocean weights  
447 in Fig. 7a. In the SST case, the land-sea  $\theta_e$  gradient is negative on the east coast of Africa

448 (along the blue arrow in Fig. 8b), and positive on the west coast Sahel region of Africa  
449 (black arrow). These  $\theta_e$  gradients again have corresponding changes in precipitation and  
450 RWS forcings: a decrease in precipitation (Figs. 2b,d) and negative RWS forcing on the  
451 east coast of Africa and an increase in precipitation and positive RWS forcing in the west  
452 coast Sahel region of Africa. Again, this is consistent with the opposite sign of the Eastern  
453 Atlantic weight in Fig. 7b.

454 The response of the land-sea  $\theta_e$  contrast on the west coast of Africa is tied to the pre-  
455 cipitation response in the region, which arises due to a shift in the ITCZ (Fig. 2). The ITCZ  
456 shifts toward the anomalously warm hemisphere (Baker et al. 2018b): in the GHG case the  
457 ITCZ shifts northwards as the NH warms more due to having more land; in the SST case,  
458 the ITCZ shifts southwards as the Southern Hemisphere warms more due to having more  
459 ocean. Previous work has found the same sign ITCZ shifts in this region as this study finds:  
460 northwards due to greenhouse gas forcing and southwards due to global SST warming (e.g.  
461 Hoerling et al. 2006; Skinner et al. 2012). In the GHG case, on the west coast where the  
462 precipitation anomaly is negative,  $\theta_e$  decreases going from ocean to land, consistent with  
463 a decrease in convection. In the SST case, the precipitation anomaly is positive, with an  
464 increase in  $\theta_e$  from ocean to land, consistent with an increase in convection. The convec-  
465 tion responses which arise from the ITCZ shift lead to the RWS responses over the Eastern  
466 Atlantic, which are opposite in sign compared to the Western Atlantic and Indian Ocean  
467 regions in both the GHG and SST responses.

468 We identify two key coastal regions just off the east coast of continents, the east coast  
469 of South America and just off the east coast of Africa (co-located with the western part  
470 of the Indian Ocean basin), and a further region just off the west coast of Africa. Positive  
471 RWS forcing in the east coast regions associated with decreased upper-level divergence,

472 and negative RWS forcing in the west coast region associated with increased upper-level  
473 divergence, acts to force the NH stationary wave in summer.

474 The regions we identify for forcing this particular wave have been shown to be impor-  
475 tant in forcing extratropical Rossby waves in other studies. Changes in outgoing longwave  
476 radiation in observations in summer over the tropical Atlantic, coinciding with the regions  
477 where we see precipitation changes in this study, have been associated with summer cir-  
478 culation patterns over Europe (Cassou et al. 2005). The Summer East Atlantic pattern, as  
479 observed in reanalysis by Wulff et al. (2017) has an associated circumglobal wavenumber 5  
480 wave, which is linked to an anomalous tropical precipitation pattern with similarities to the  
481 precipitation patterns we find in this study: drying in the Western Atlantic and wetting over  
482 the Sahel region in Africa, producing a similar convergent forcing as we find in this study.  
483 Yasui and Watanabe (2010) also find that precipitation changes over equatorial Africa are  
484 important in forcing the observed circumglobal teleconnection (CGT, see Ding and Wang  
485 (2005)) in boreal summer. The wave we observe is not an excitation of the CGT: the wave  
486 centres we observe do not coincide with the CGT, and as demonstrated in Section 4, the  
487 wave we force is not an excitation of a wave present in the background state. However, the  
488 fact that studies on the CGT find similar key forcing regions as this study suggests that these  
489 regions are important generally in forcing boreal summer Rossby waves. As well as equa-  
490 torial Africa, the Indian summer monsoon region (which includes the area of ocean just off  
491 the east coast of Africa) has also been found important in forcing aspects of the CGT (Ding  
492 and Wang 2007), and other NH teleconnection patterns (Lin 2009).

493 The opposing effects of radiative forcing versus sea surface warming have important  
494 implications on regional climates and extremes. Framed in terms of a global mean tem-  
495 perature target, the changes in regional climates and extremes depend significantly on the  
496 climate sensitivity (defined as the global mean temperature warming due to a doubling of

497 atmospheric CO<sub>2</sub> concentrations), which is subject to large uncertainties (IPCC 2014). If the  
498 Earth has a low climate sensitivity, the temperature target may be met, but with correspond-  
499 ing dangerous changes in certain regional extremes (Baker et al. 2018a), due to increases  
500 in tropical precipitation over land and the wavelike temperature increase pattern over the  
501 NH. For higher climate sensitivities, less CO<sub>2</sub> would be emitted to reach the same temper-  
502 ature target, and so the opposing effect of the sea surface warming would balance out the  
503 direct CO<sub>2</sub> effect to a greater extent. If the climate sensitivity is very high, the direct CO<sub>2</sub>  
504 effect will be relatively unimportant compared to the sea surface warming effect, leading  
505 to drying over the land in the tropics, and different regions (those under the anticyclonic  
506 regions of the stationary wave pattern) experiencing increases in heat extremes. Geoengi-  
507 neering techniques aiming to tackle climate change impacts without removing CO<sub>2</sub> would  
508 exacerbate the direct CO<sub>2</sub> effect when stabilising at a temperature target as the techniques  
509 would reduce global mean temperature without removing CO<sub>2</sub>. Ultimately, the interplay of  
510 the two opposing effects will be dictated by the Earth's climate sensitivity, and further work  
511 is need to quantify the exact magnitudes of the direct CO<sub>2</sub> and sea surface warming effects  
512 on changes in precipitation and on the forced stationary wave.

513 On the question of the interaction between the direct CO<sub>2</sub> effect and sea surface warming  
514 effect, Lambert et al. (2011) found no substantial nonlinearities in indices of atmospheric  
515 circulation when the doubling of CO<sub>2</sub> and spatially uniform SST warming were added to an  
516 AGCM. Deser and Phillips (2009) also observe a high degree of linearity in the response to  
517 direct CO<sub>2</sub> effects and sea surface warming in atmospheric circulation trends during 1950-  
518 2000 simulated in an AGCM. This suggests the opposing effects on circulation may combine  
519 linearly as in the barotropic modelling experiments in this study, although further work is  
520 needed to confirm this.

521 The SST forcing model results presented here rely on one global warming pattern change,  
522 and the direct CO<sub>2</sub> runs all have the same fixed SST pattern. However, it has been suggested  
523 that the pattern of SST warming plays an important part in certain regional circulation re-  
524 sponses (He and Soden 2015) and the tropical precipitation response to SST warming (Chad-  
525 wick 2016). The robustness of the wave response in the AMIP4K response suggests that the  
526 wave is forced by changes in mean SST warming, but further work investigating the uncer-  
527 tainty arising from the SST pattern change is needed before quantitative predictions about  
528 the opposing effects of radiative forcing and sea surface warming can be made.

529 There are several other possible contributing factors to the direct CO<sub>2</sub> effect, which re-  
530 quire further study to quantify. Radiative changes in clouds have been linked to circulation  
531 changes (Voigt and Shaw 2015) and large scale cloud cover changes over the NH in sum-  
532 mer are associated with the direct CO<sub>2</sub> effect (Richardson et al. 2016), with a decrease in  
533 cloud cover over regions that see strong increases in temperature due to CO<sub>2</sub>. However, de-  
534 termining the causality between the cloud cover changes and the temperature changes is a  
535 complex issue. One possibility is that the anticyclonic regions of the forced stationary waves  
536 cause cloud to be less prevalent in these regions, adding to the increases in local tempera-  
537 ture. Midlatitude stationary wave changes can also be affected by changes in the zonal mean  
538 westerlies in the sub-tropical upper troposphere (Simpson et al. 2016). We do not observe  
539 this effect in this study, and Grise and Polvani (2014) show that whilst there are differing  
540 effects on the zonal circulation under direct radiative forcing and sea surface warming, the  
541 effects are not opposite. However, with large variations among future predictions in zonal  
542 wind changes (Simpson et al. 2014), this effect could be important in dictating the charac-  
543 teristics of the forced stationary wave.

544 A modelling intercomparison project as part of the new CMIP6 ensemble, The Cloud  
545 Feedback Model Intercomparison Project Phase 3 (CFMIP3) (Webb et al. 2017), consists

546 of AMIP style simulations designed to investigate effects on clouds and circulation of CO<sub>2</sub>  
547 radiative effects, physiological effects, SST uniform warming and SST pattern effects. Chad-  
548 wick et al. (2017) use several models from CFMIP3 to demonstrate in winter that the phys-  
549 iological effect and SST pattern change play important roles in the hydrological cycle and  
550 European circulation changes. The full CFMIP3 ensemble will enable more quantitative pre-  
551 dictions and analysis surrounding the opposing effects of radiative forcing and sea surface  
552 warming in summer to be carried out.

553 **6 Conclusions**

554 Using results from three GCMs and CMIP5, we have shown here that there are opposing  
555 effects of direct CO<sub>2</sub> forcing and sea surface warming on tropical precipitation and forced  
556 summer NH stationary waves. The direct effect of CO<sub>2</sub> forcing leads to a drying over the  
557 land and wetting over the ocean in the tropics in boreal summer in key forcing locations.  
558 This forces a wavenumber 5 stationary wave pattern over the NH. We observe the opposite  
559 precipitation response due to sea surface warming, which forces the same wave over the NH  
560 but with opposite sign. The three key locations for forcing the summer wave are found to be  
561 the Western Atlantic, Eastern Atlantic and in the Indian Ocean off the east coast of Africa.

562 This study has important implications for changes in regional climates and extremes  
563 which depend heavily on the Earth's climate sensitivity and land-sea temperature contrast  
564 response. The opposing effects of radiative forcing and sea surface warming and their rela-  
565 tive importance at a specific global mean temperature are determined by how much CO<sub>2</sub> is  
566 emitted to reach such a temperature. A low climate sensitivity means a greater contribution  
567 from the direct CO<sub>2</sub> effect, i.e. enhanced precipitation (and precipitation extremes (Baker  
568 et al. 2018a)) over tropical land, and increases in heat extremes under the anticyclonic cen-

tres of the CO<sub>2</sub> forced stationary wave. On the other hand, a high climate sensitivity means a greater contribution from the sea surface warming effect, i.e. reduced precipitation over tropical land, and increases in heat extremes shifted to the cyclonic centres of the CO<sub>2</sub> forced stationary wave, which are anticyclonic for the sea surface warming forced wave. The future change in land-sea temperature contrast will also play an important role in determining the balance between the opposing effects. A larger land-sea temperature contrast response could lead to a larger forcing of the direct CO<sub>2</sub> wave, compared to a smaller response. The relative magnitude of the combination of the opposing effects of directive radiative forcing and sea surface warming is still uncertain due to uncertainty in the Earth's climate sensitivity and land-sea temperature contrast response (Byrne and O'Gorman 2013). This study points to the need to reduce the uncertainties in the climate sensitivity and land-sea contrast response to better constrain how regional precipitation and temperature patterns will change under global warming.

## 582 Appendix: Equivalent potential temperature

583 To analyse differences in the response to SST versus CO<sub>2</sub> forcing, we compute the equivalent potential temperature,  $\theta_e$ , the temperature a parcel of air would reach if brought adiabatically to a standard reference pressure (taken to be 1000 hPa) and all the water vapour in the parcel were to condense, releasing its latent heat (Amabaum 2010). Following Bolton 586 (1980),  $\theta_e$  can be calculated as follows:

$$\theta_e = \theta_L \exp \left[ \left( \frac{3036}{T_L} - 1.78 \right) r (1 + 0.448r) \right]. \quad (\text{A1})$$

588  $\theta_L$  is the dry potential temperature (in Kelvin) at the lifted condensation level,

$$\theta_L = T \left( \frac{p_0}{p - e} \right)^{\kappa_d} \left( \frac{T}{T_L} \right)^{0.28r}. \quad (\text{A2})$$

<sup>589</sup>  $T_L$  is the approximate temperature (in Kelvin) at the lifted condensation level,

$$T_L = \frac{1}{\frac{1}{T_d - 56} + \frac{\ln(T/T_d)}{800}} + 56. \quad (\text{A3})$$

<sup>590</sup> Here,  $T$  is the temperature (in Kelvin) of the air at pressure  $p$  (in hPa),  $p_0$  is a standard  
<sup>591</sup> reference pressure (taken to be 1000 hPa) and  $\kappa_d = R_d/c_{pd} = 0.2854$  is the ratio of the spe-  
<sup>592</sup> cific gas constant to the specific heat of dry air at constant pressure.  $e$  is the water vapour  
<sup>593</sup> pressure in hPa, calculated from relative humidity by  $RH = \frac{e}{e_s} \times 100\%$ , where the satu-  
<sup>594</sup> rated water pressure  $e_s(T) = 6.1094 \exp \left[ \frac{17.625(T-273.15)}{T-30.11} \right]$  (Alduchov and Eskridge 1996).  
<sup>595</sup>  $r = 0.622 \frac{e}{p-e}$  is the mixing ratio of water vapour per mass (kg/kg).  $T_d$  is the dew point tem-  
<sup>596</sup> perature which can be calculated from the relative humidity  $RH = e_s(T_d)/e_s(T)$  (Amabaum  
<sup>597</sup> 2010).

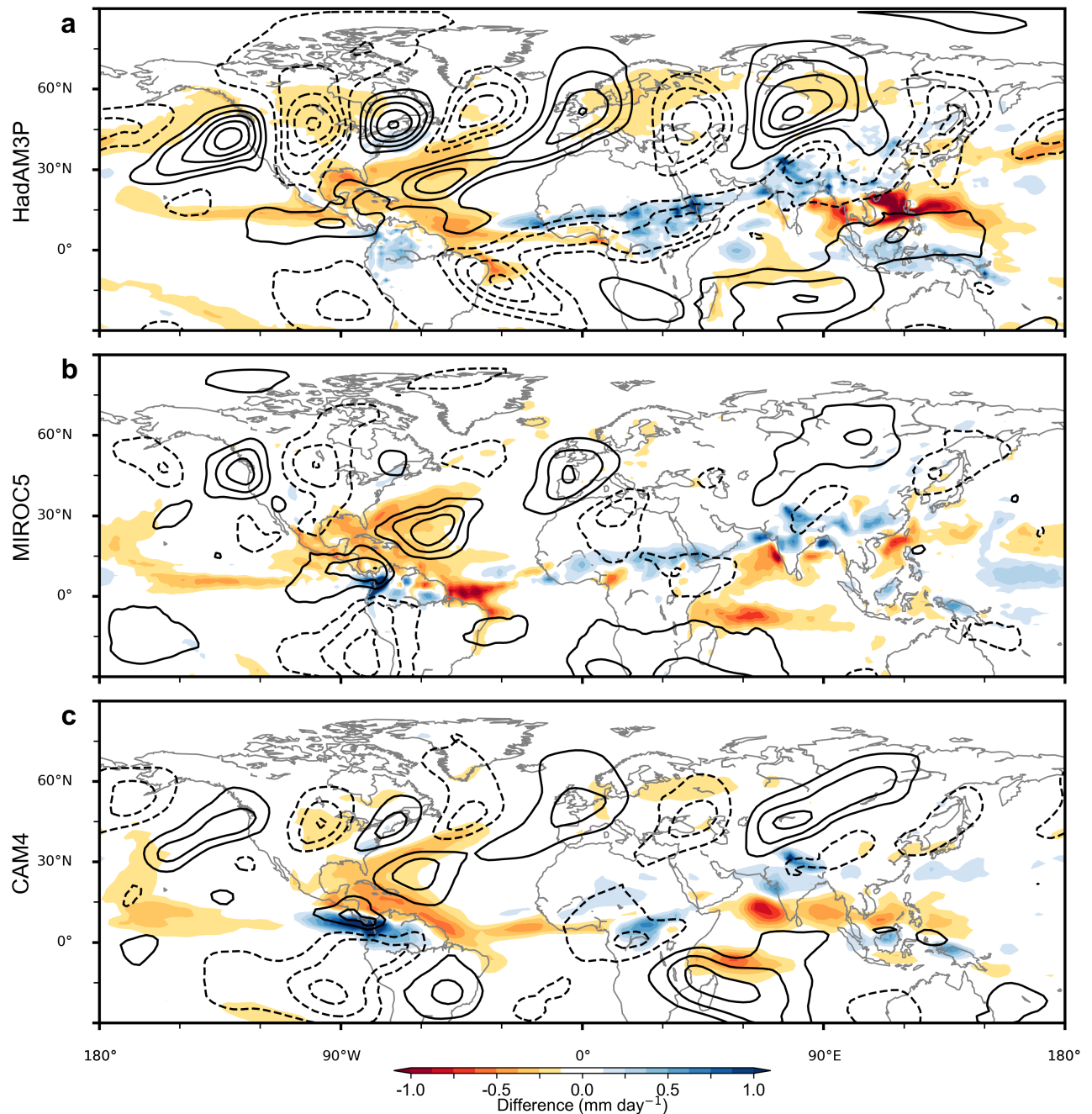


**Fig. 1** Responses of the different models to CO<sub>2</sub> forcing. (a) HadAM3P CO<sub>2</sub>, (b) MIROC5 CO<sub>2</sub> and (c) CAM4 CO<sub>2</sub>. Contours show the JJA 200 hPa meridional wind response (interval: 0.2 ms<sup>-1</sup> with the zero contour suppressed), colours show the JJA precipitation response. The CAM4 wind and precipitation responses have been multiplied subjectively by 2.5 to be plotted on the same scale as the other two model responses.

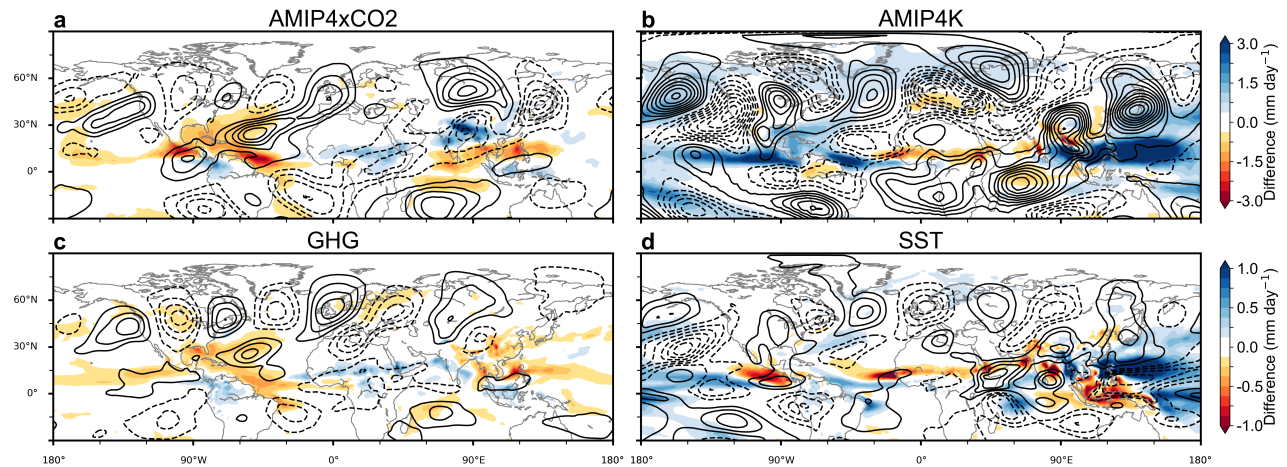


**Fig. 2** Responses to GHG and SST forcing. (a) AMIP4xCO<sub>2</sub>, (b) AMIP4K, (c) HadAM3P GHG and (d) HadAM3P SST. Contours show the JJA 200 hPa meridional wind response (interval: 0.4 ms<sup>-1</sup> (a,b) and 0.2 ms<sup>-1</sup> (c,d) with the zero contour suppressed), colours show the JJA precipitation response.

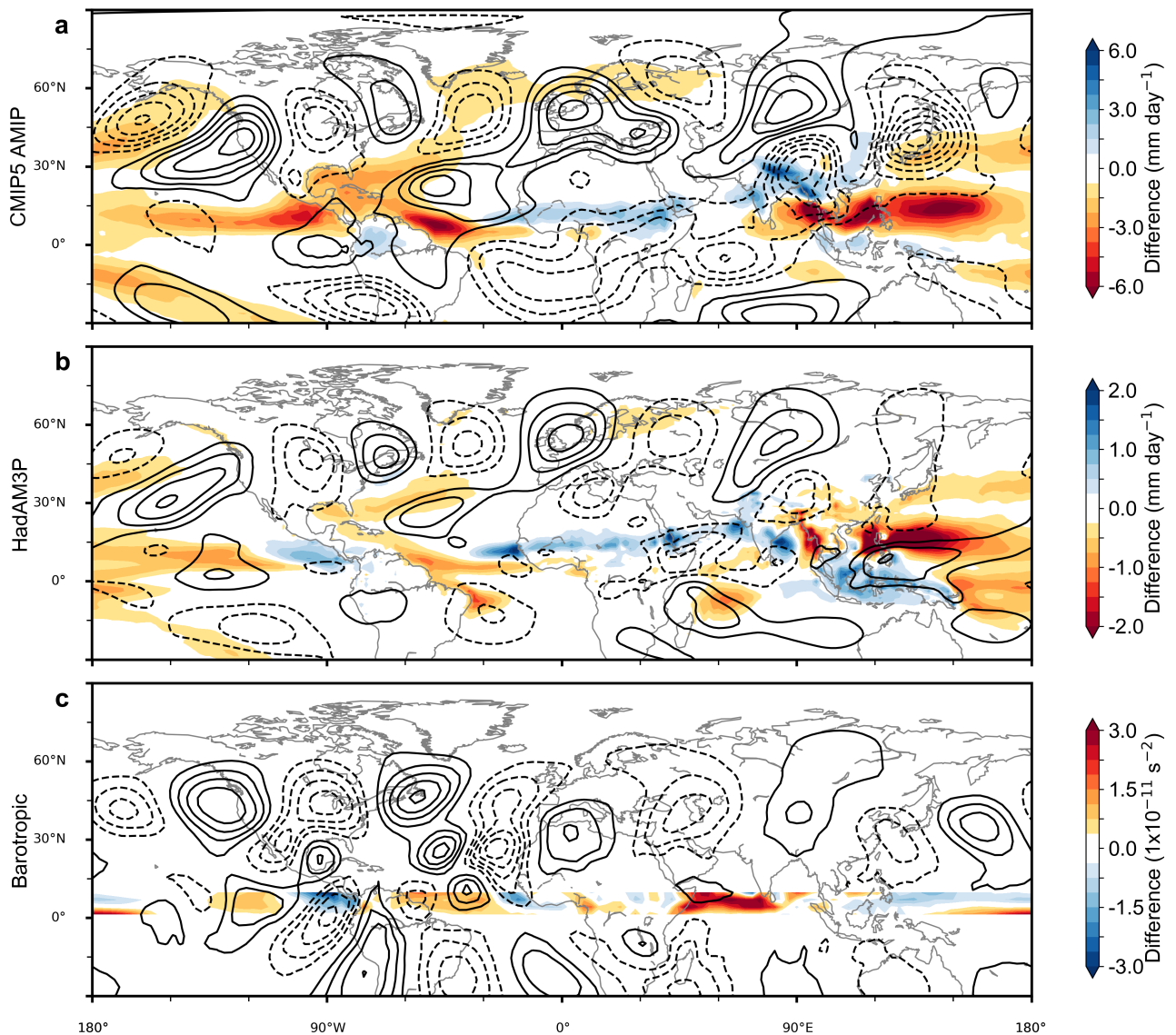


**Fig. 3** Summary of the responses to forcing in the different experiments. (a) summary of the CMIP5 AMIP experiments showing difference the between  $4\times\text{CO}_2$  and AMIP4K ensemble mean responses, (b) summary of the Hadley experiments showing the difference of GHG and SST ensemble mean responses. Contours show the JJA 200 hPa meridional wind response (interval:  $0.8 \text{ ms}^{-1}$  (a) and  $0.4 \text{ ms}^{-1}$  (b) with the zero contour suppressed), colours show the JJA precipitation response. (c) summary of the barotropic modelling experiments. Colours show the difference between the anomalous May RWS forcings in the GHG and SST ensembles. Contours show the difference between the model response when forced with the anomalous GHG RWS and when forced with the anomalous SST RWS (interval:  $0.3 \text{ ms}^{-1}$  with the zero contour suppressed).

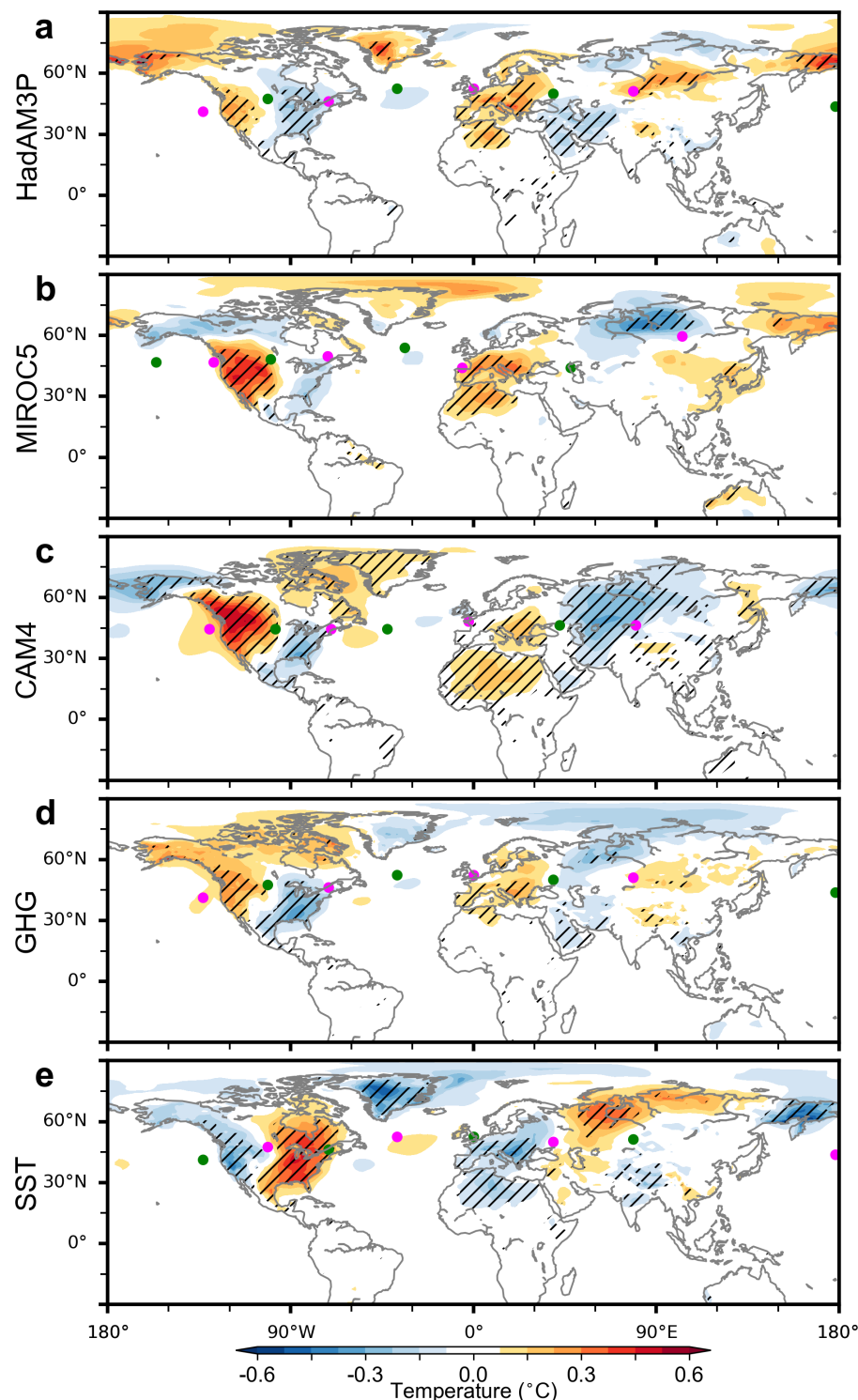


**Fig. 4** Effect of the hemispheric wave on summer temperatures. JJA daily mean temperatures regressed onto the standardized circulation index for (a) HadAM3P CO<sub>2</sub>, (b) MIROC5 CO<sub>2</sub>, (c) CAM4 CO<sub>2</sub>, (d) HadAM3P GHG and (e) HadAM3P SST. The hatching shows where the regression is significant at the 5% level using a two-sided Wald Test. Pink and green dots mark the positive and negative wave centres respectively used to create the circulation index for each ensemble.

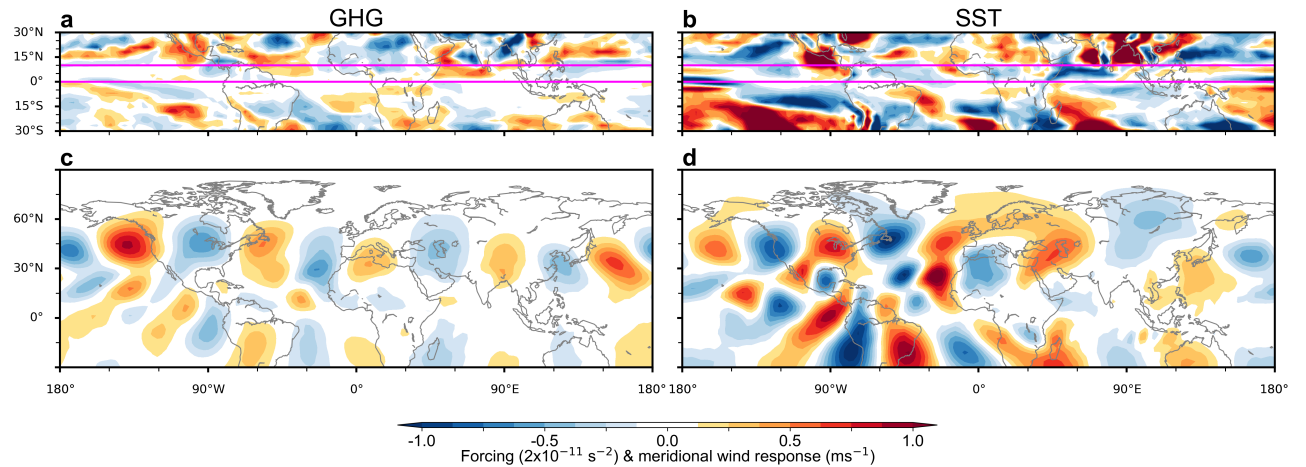


**Fig. 5** Barotropic model forcing and response. May Rossby wave source forcing from HadAM3P (a) GHG and (c) SST runs. The pink box demarcates the region used to force the barotropic model ( $0^{\circ}$ - $10^{\circ}$ N). Barotropic model meridional wind response averaged from day 16-20 for (b) the GHG forcing and (d) the SST forcing. Both cases use the NAT ensemble mean June 200 hPa vorticity as the background state.

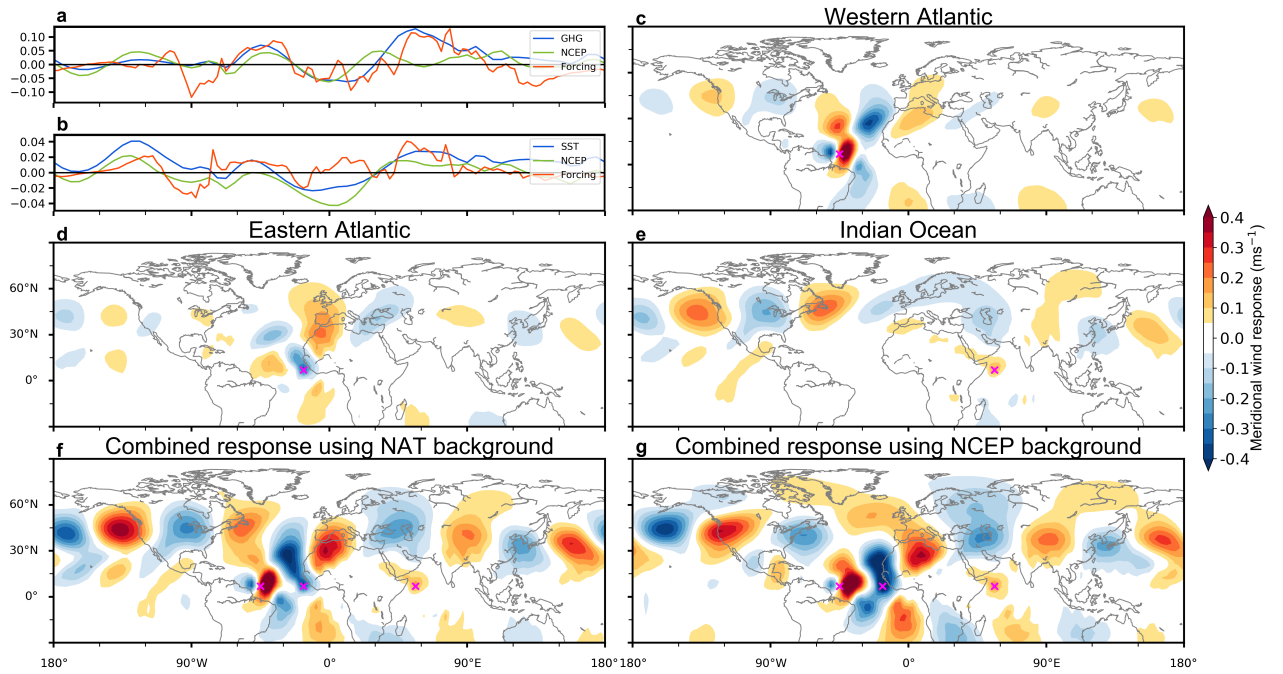


**Fig. 6** Idealised barotropic model results. Weights from idealised patch experiments for NAT and NCEP backgrounds and HadAM3P Rossby wave source for (a) GHG ensemble response and (b) SST ensemble response. Rossby wave source is averaged over  $0^{\circ}$ - $10^{\circ}$ N and then normalised so its maximum corresponds to the June weight maximum. The weights in the SST case have been multiplied by -1. Idealised meridional wind responses are shown for (c) West Atlantic, (d) East Atlantic and (e) Indian Ocean forcing patches (location marked by pink cross). Combined response of Western and Eastern Atlantic and Indian Ocean forcings with (f) NAT background state and (g) NCEP background state.

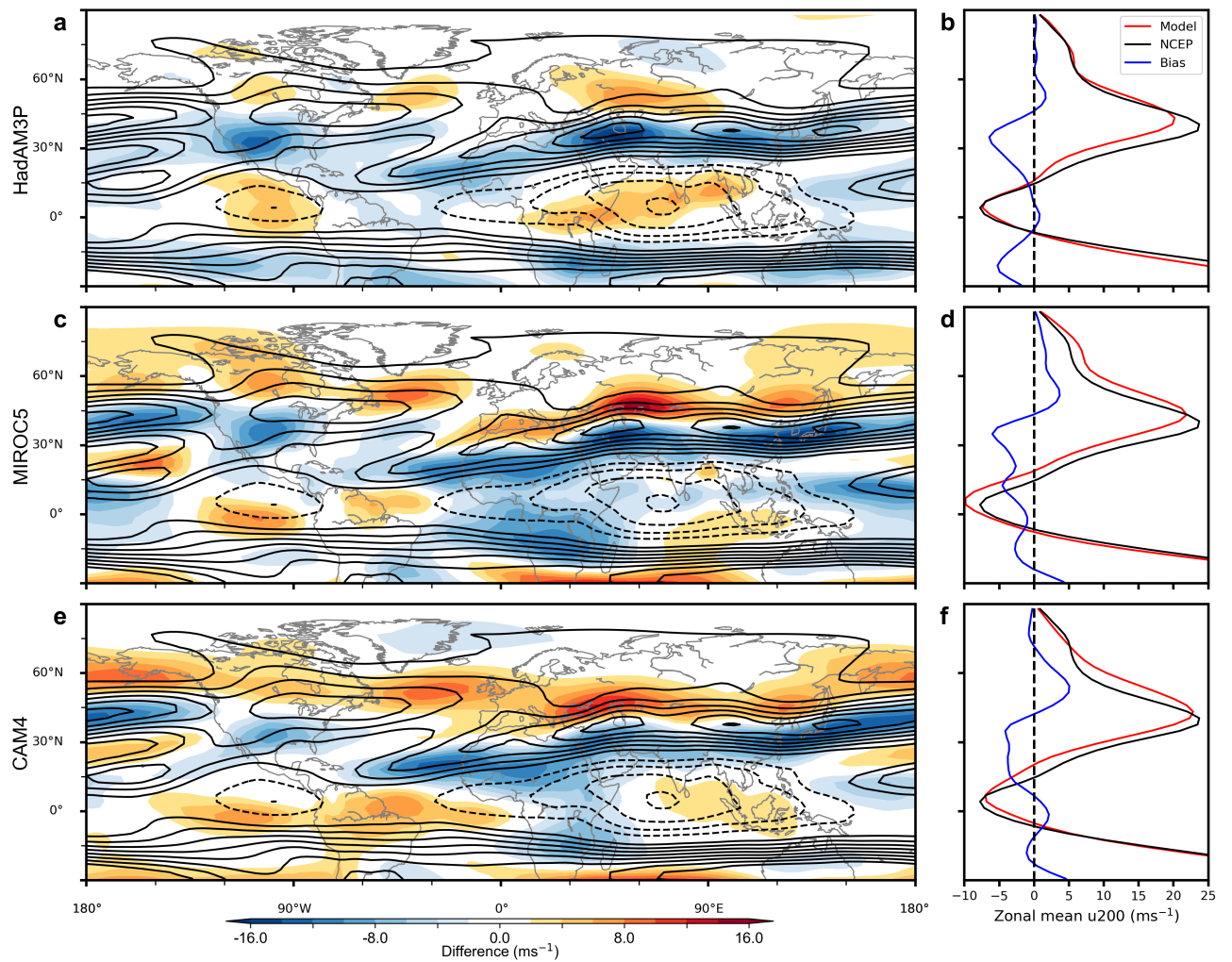


**Fig. 7** Model zonal wind biases for June in (a,b) HadAM3P, (c,d) MIROC5 and (e,f) CAM4. Contours in (a,c,e) show the June 1979-2015 200 hPa zonal wind from the NCEP 2 reanalysis (contours at 5  $\text{ms}^{-1}$  intervals with the zero contour suppressed). Colours in (a,c,e) show the difference between the June 200 hPa zonal wind in the model (2006-2015) and the NCEP 2 reanalysis (1979-2015). (b,d,f) show the zonal mean zonal winds and the bias, defined as the difference between the model and NCEP 2 reanalysis means, shown in blue.

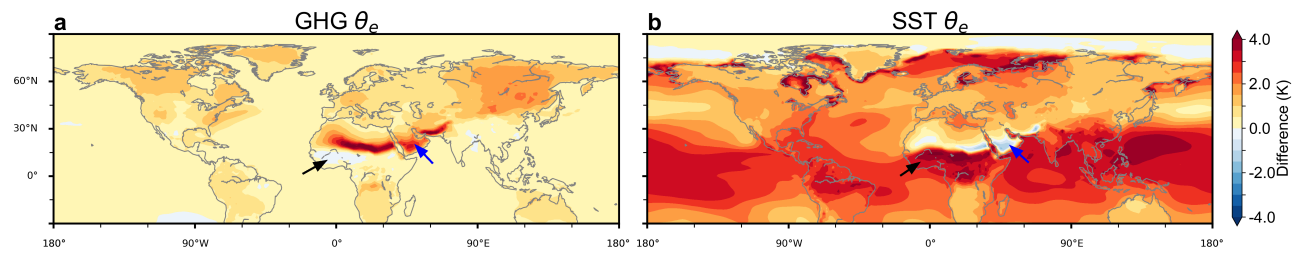


**Fig. 8** Responses to GHG and SST forcing.  $\theta_e$  response for (a) HadAM3P GHG and (b) HadAM3P SST. See the Appendix for details of calculation.

**Table 1** Summary of ensembles and their setups.

<i>Experiment</i>	<i>Ensemble</i>	<i>Model</i>	<i>Resolution</i>	<i>SST</i>	<i>CO<sub>2</sub>[ppm]</i>
1.5°C	LCO <sub>2</sub>	HadAM3P	1.25°×1.875°	1.5°C	395.8
	HCO <sub>2</sub>	HadAM3P	1.25°×1.875°	1.5°C	550.0
	LCO <sub>2</sub>	MIROC5	1.4°×1.4°	1.5°C	395.8
	HCO <sub>2</sub>	MIROC5	1.4°×1.4°	1.5°C	550.0
	LCO <sub>2</sub>	CAM4	1.9°×2.5°	1.5°C	379.0
Hadley	HCO <sub>2</sub>	CAM4	1.9°×2.5°	1.5°C	423.1
	NAT	HadAM3P	1.25°×1.875°	Natural	284.4
	GHG	HadAM3P	1.25°×1.875°	Natural	390.4
CMIP5	SST	HadAM3P	1.25°×1.875°	Historical	284.4
	AMIP	see text	various	Historical	Historical
	AMIP4xCO <sub>2</sub>	see text	various	Historical	4×Historical
	AMIP4K	see text	various	Historical+4K	Historical

598 **Acknowledgements** This work was supported by the Natural Environment Research Council (grant NE/L002612/1  
 599 and NERC SummerTIME project, grant NE/M005887/1). H. Shiogama was supported by the TOUGOU  
 600 project of MEXT, Japan and by the Environment Research and Technology Development Fund (2-1702) of  
 601 the Environmental Restoration and Conservation Agency, Japan. The authors thank Urs Beyerle for making  
 602 the data from CAM4 available. This research used science gateway resources of the National Energy Research  
 603 Scientific Computing Center, a DOE Office of Science User Facility supported by the Office of Science of  
 604 the U.S. Department of Energy under Contract No. DE-AC02-05CH11231. We would like to thank our col-  
 605 leagues at the Oxford eResearch Centre: A. Bowery, M. Rashid, S. Sparrow, P. Uhe and D. Wallom for their  
 606 technical expertise. We would like to thank the Met Office Hadley Centre PRECIS team for their technical  
 607 and scientific support for the development and application of weather@Home. Finally, we would like to thank  
 608 all of the volunteers who have donated their computing time to climateprediction.net and weather@home.

---

**609 References**

- 610 Alduchov OA, Eskridge RE (1996) Improved Magnus Form Approx-  
611 imation of Saturation Vapor Pressure. *J Appl Meteorol* 35(4):601–  
612 609, DOI 10.1175/1520-0450(1996)035;0601:IMFAOS;2.0.CO;2,  
613 URL <http://journals.ametsoc.org/doi/abs/10.1175/1520-0450%281996%29035%3C0601%3AIMFAOS%3E2.0.CO%3B2>
- 614 Allen M (1999) Do-it-yourself climate prediction. *Nature* 401(6754):642–642, DOI  
615 10.1038/44266, URL <http://www.nature.com/doifinder/10.1038/44266>
- 616 Ambaum MHP (2010) Thermal Physics of the Atmosphere. John Wiley & Sons, Ltd, DOI  
617 10.1002/9780470710364, URL <http://doi.wiley.com/10.1002/9780470710364>
- 618 Ambrizzi T, Hoskins BJ, Hsu HH (1995) Rossby Wave Propaga-  
619 tion and Teleconnection Patterns in the Austral Winter. *J Atmos Sci*  
620 52(21):3661–3672, DOI 10.1175/1520-0469(1995)052;3661:RWPATP;2.0.CO;2,  
621 URL <http://journals.ametsoc.org/doi/abs/10.1175/1520-0469%281995%29052%3C3661%3ARWPATP%3E2.0.CO%3B2>
- 622 Andrews T, Forster PM, Gregory JM (2009) A Surface Energy Perspective on  
623 Climate Change. *J Clim* 22(10):2557–2570, DOI 10.1175/2008JCLI2759.1, URL  
624 <http://journals.ametsoc.org/doi/abs/10.1175/2008JCLI2759.1>
- 625 Baker HS, Millar RJ, Karoly DJ, Beyerle U, Guillod BP, Mitchell D, Shiogama H, Sparrow  
626 S, Woollings T, Allen MR (2018a) Higher CO<sub>2</sub> concentrations increase extreme event  
627 risk in a 1.5C world. *Nat Clim Chang* 8(7):604–608, DOI 10.1038/s41558-018-0190-1,  
628 URL <http://www.nature.com/articles/s41558-018-0190-1>
- 629 Baker HS, Mbengue C, Woollings T (2018b) Seasonal Sensitivity of the Hadley  
630 Cell and Cross-Hemispheric Responses to Diabatic Heating in an Idealized
- 631

- 633 GCM. Geophys Res Lett 45(5):2533–2541, DOI 10.1002/2018GL077013, URL  
634 <http://doi.wiley.com/10.1002/2018GL077013>
- 635 Barsugli JJ, Sardeshmukh PD (2002) Global atmospheric sensitivity to  
636 tropical SST anomalies throughout the Indo-Pacific basin. J Clim  
637 15(23):3427–3442, DOI 10.1175/1520-0442(2002)015;3427:GASTTS;2.0.CO;2,  
638 URL [http://journals.ametsoc.org/doi/abs/10.1175/1520-0442\(2002\)015%3C3427%3AGASTTS%3E2.0.CO%3B2](http://journals.ametsoc.org/doi/abs/10.1175/1520-0442(2002)015%3C3427%3AGASTTS%3E2.0.CO%3B2)
- 639 Bieli M, Pfahl S, Wernli H (2015) A Lagrangian investigation of hot and cold temperature  
640 extremes in Europe. Q J R Meteorol Soc 141(686):98–108, DOI 10.1002/qj.2339, URL  
641 <http://doi.wiley.com/10.1002/qj.2339>
- 642 Bolton D (1980) The Computation of Equivalent Potential Temperature. Mon Weather Rev  
643 108(7):1046–1053, DOI 10.1175/1520-0493(1980)108;1046:TCOEPT;2.0.CO;2,  
644 URL <http://journals.ametsoc.org/doi/abs/10.1175/1520-0493%281980%29108%3C1046%3ATCOEPT%3E2.0.CO%3B2>
- 645 Bony S, Bellon G, Klocke D, Sherwood S, Fermeipin S, Denvil S (2013) Robust direct effect  
646 of carbon dioxide on tropical circulation and regional precipitation. Nat Geosci 6(6):447–  
647 451, DOI 10.1038/ngeo1799, URL <http://www.nature.com/doifinder/10.1038/ngeo1799>
- 648 Branstator G (2002) Circumglobal Teleconnections, the Jet Stream  
649 Waveguide, and the North Atlantic Oscillation. J Clim 15(14):1893–  
650 1910, DOI 10.1175/1520-0442(2002)015;1893:CTTJSW;2.0.CO;2,  
651 URL <http://journals.ametsoc.org/doi/abs/10.1175/1520-0442%282002%29015%3C1893%3ACTTJSW%3E2.0.CO%3B2>
- 652 Byrne MP, O’Gorman PA (2013) Link between land-ocean warming contrast  
653 and surface relative humidities in simulations with coupled climate mod-  
654 els. Geophys Res Lett 40(19):5223–5227, DOI 10.1002/grl.50971, URL

- 658      <http://doi.wiley.com/10.1002/grl.50971>
- 659    Cao L, Bala G, Caldeira K (2012) Climate response to changes in atmospheric car-  
660    bon dioxide and solar irradiance on the time scale of days to weeks. Environ Res  
661    Lett 7(3):034015, DOI 10.1088/1748-9326/7/3/034015, URL <http://stacks.iop.org/1748-9326/7/i=3/a=034015?key=crossref.b4a65cfba7f3fd7d4078736920eed250>
- 662    Cassou C, Terray L, Phillips AS (2005) Tropical Atlantic Influence on Euro-  
663    pean Heat Waves. J Clim 18(15):2805–2811, DOI 10.1175/JCLI3506.1, URL  
664    <http://journals.ametsoc.org/doi/abs/10.1175/JCLI3506.1>
- 665    Chadwick R (2016) Which Aspects of CO<sub>2</sub> Forcing and SST Warming Cause  
666    Most Uncertainty in Projections of Tropical Rainfall Change over Land  
667    and Ocean? J Clim 29(7):2493–2509, DOI 10.1175/JCLI-D-15-0777.1, URL  
668    <http://journals.ametsoc.org/doi/10.1175/JCLI-D-15-0777.1>
- 669    Chadwick R, Good P, Andrews T, Martin G (2014) Surface warming patterns drive tropical  
670    rainfall pattern responses to CO<sub>2</sub> forcing on all timescales. Geophys Res Lett 41(2):610–  
671    615, DOI 10.1002/2013GL058504, URL <http://doi.wiley.com/10.1002/2013GL058504>
- 672    Chadwick R, Douville H, Skinner CB (2017) Timeslice experiments for understanding  
673    regional climate projections: applications to the tropical hydrological cycle and Euro-  
674    pean winter circulation. Clim Dyn 49(9-10):3011–3029, DOI 10.1007/s00382-016-3488-  
675    6, URL <http://link.springer.com/10.1007/s00382-016-3488-6>
- 676    Compo GP, Sardeshmukh PD (2009) Oceanic influences on recent continental  
677    warming. Clim Dyn 32(2-3):333–342, DOI 10.1007/s00382-008-0448-9, URL  
678    <http://link.springer.com/10.1007/s00382-008-0448-9>
- 679    Deser C, Phillips AS (2009) Atmospheric Circulation Trends, 1950–2000: The  
680    Relative Roles of Sea Surface Temperature Forcing and Direct Atmospheric  
681    Radiative Forcing. J Clim 22(2):396–413, DOI 10.1175/2008JCLI2453.1, URL  
682    <http://journals.ametsoc.org/doi/abs/10.1175/2008JCLI2453.1>

- 683      <http://journals.ametsoc.org/doi/abs/10.1175/2008JCLI2453.1>
- 684    Ding Q, Wang B (2005) Circumglobal Teleconnection in the Northern Hemi-  
685    sphere Summer\*. *J Clim* 18(17):3483–3505, DOI 10.1175/JCLI3473.1, URL  
686    <http://journals.ametsoc.org/doi/abs/10.1175/JCLI3473.1>
- 687    Ding Q, Wang B (2007) Intraseasonal Teleconnection between the Summer Eurasian Wave  
688    Train and the Indian Monsoon\*. *J Clim* 20(15):3751–3767, DOI 10.1175/JCLI4221.1,  
689    URL <http://journals.ametsoc.org/doi/abs/10.1175/JCLI4221.1>
- 690    Dong B, Sutton R (2015) Dominant role of greenhouse-gas forcing in the recovery  
691    of Sahel rainfall. *Nat Clim Chang* 5(8):757–760, DOI 10.1038/nclimate2664, URL  
692    <http://www.nature.com/doifinder/10.1038/nclimate2664>
- 693    Dong B, Gregory JM, Sutton RT (2009) Understanding Land-Sea Warming  
694    Contrast in Response to Increasing Greenhouse Gases. Part I: Transient Ad-  
695    justment. *J Clim* 22(11):3079–3097, DOI 10.1175/2009JCLI2652.1, URL  
696    <http://journals.ametsoc.org/doi/abs/10.1175/2009JCLI2652.1>
- 697    Dong B, Sutton RT, Chen W, Liu X, Lu R, Sun Y (2016) Abrupt summer warming and  
698    changes in temperature extremes over Northeast Asia since the mid-1990s: Drivers and  
699    physical processes. *Adv Atmos Sci* 33(9):1005–1023, DOI 10.1007/s00376-016-5247-3,  
700    URL <http://link.springer.com/10.1007/s00376-016-5247-3>
- 701    Donlon CJ, Martin M, Stark J, Roberts-Jones J, Fiedler E, Wimmer W (2012)  
702    The Operational Sea Surface Temperature and Sea Ice Analysis (OSTIA) sys-  
703    tem. *Remote Sens Environ* 116:140–158, DOI 10.1016/J.RSE.2010.10.017, URL  
704    <https://www.sciencedirect.com/science/article/pii/S0034425711002197>
- 705    Folland CK, Sexton DMH, Karoly DJ, Johnson CE, Rowell DP, Parker DE  
706    (1998) Influences of anthropogenic and oceanic forcing on recent climate  
707    change. *Geophys Res Lett* 25(3):353–356, DOI 10.1029/97GL03701, URL

- 708        <http://doi.wiley.com/10.1029/97GL03701>
- 709    Gent PR, Danabasoglu G, Donner LJ, Holland MM, Hunke EC, Jayne  
710      SR, Lawrence DM, Neale RB, Rasch PJ, Vertenstein M, Worley PH,  
711      Yang ZL, Zhang M (2011) The Community Climate System Model Ver-  
712      sion 4. *J Clim* 24(19):4973–4991, DOI 10.1175/2011JCLI4083.1, URL  
713      <http://journals.ametsoc.org/doi/abs/10.1175/2011JCLI4083.1>
- 714    Gordon C, Cooper C, Senior CA, Banks H, Gregory JM, Johns TC, Mitchell JFB, Wood RA  
715      (2000) The simulation of SST, sea ice extents and ocean heat transports in a version of  
716      the Hadley Centre coupled model without flux adjustments. *Clim Dyn* 16(2-3):147–168,  
717      DOI 10.1007/s003820050010, URL <http://link.springer.com/10.1007/s003820050010>
- 718    Grise KM, Polvani LM (2014) The response of midlatitude jets to increased  
719      CO<sub>2</sub> : Distinguishing the roles of sea surface temperature and direct radiative  
720      forcing. *Geophys Res Lett* 41(19):6863–6871, DOI 10.1002/2014GL061638, URL  
721      <http://doi.wiley.com/10.1002/2014GL061638>
- 722    Guillod BP, Jones RG, Bowery A, Haustein K, Massey NR, Mitchell DM, Otto FEL, Spar-  
723      row SN, Uhe P, Wallom DCH, Wilson S, Allen MR (2017) weather@home 2: vali-  
724      dation of an improved global-regional climate modelling system. *Geosci Model Dev*  
725      10(5):1849–1872, DOI 10.5194/gmd-10-1849-2017, URL <https://www.geosci-model->  
726      dev.net/10/1849/2017/
- 727    Haarsma RJ, Selten F (2012) Anthropogenic changes in the Walker circulation  
728      and their impact on the extra-tropical planetary wave structure in the Northern  
729      Hemisphere. *Clim Dyn* 39(7-8):1781–1799, DOI 10.1007/s00382-012-1308-1, URL  
730      <http://link.springer.com/10.1007/s00382-012-1308-1>
- 731    Haustein K, Otto FEL, Uhe P, Schaller N, Allen MR, Hermanson L, Chris-  
732      tidis N, McLean P, Cullen H (2016) Real-time extreme weather event at-

- 733 tribution with forecast seasonal SSTs. Environ Res Lett 11(6):064006,  
734 DOI 10.1088/1748-9326/11/6/064006, URL <http://stacks.iop.org/1748-9326/11/i=6/a=064006?key=crossref.3f0585e9af9b6a8e6e4ab5eaf240b920>
- 735  
736 He J, Soden BJ (2015) Anthropogenic Weakening of the Tropical Circula-  
737 tion: The Relative Roles of Direct CO<sub>2</sub> Forcing and Sea Surface Tempera-  
738 ture Change. J Clim 28(22):8728–8742, DOI 10.1175/JCLI-D-15-0205.1, URL  
739 <http://journals.ametsoc.org/doi/10.1175/JCLI-D-15-0205.1>
- 740 Held IM, Soden BJ (2006) Robust Responses of the Hydrological Cycle to  
741 Global Warming. J Clim 19(21):5686–5699, DOI 10.1175/JCLI3990.1, URL  
742 <http://journals.ametsoc.org/doi/abs/10.1175/JCLI3990.1>
- 743 Hoerling M, Hurrell J, Eischeid J, Phillips A (2006) Detection and Attribution of Twentieth-  
744 Century Northern and Southern African Rainfall Change. J Clim 19(16):3989–4008, DOI  
745 10.1175/JCLI3842.1, URL <http://journals.ametsoc.org/doi/abs/10.1175/JCLI3842.1>
- 746 Hoskins BJ, Ambrizzi T (1993) Rossby Wave Propagation on a Re-  
747 alistic Longitudinally Varying Flow. J Atmos Sci 50(12):1661–  
748 1671, DOI 10.1175/1520-0469(1993)050;1661:RWPOAR;2.0.CO;2,  
749 URL <http://journals.ametsoc.org/doi/abs/10.1175/1520-0469%281993%29050%3C1661%3ARWPOAR%3E2.0.CO%3B2>
- 750  
751 IPCC (2014) Climate change 2013: The physical science basis. Cambridge University Press,  
752 2013b, URL <http://www.epa-pictaural.com/ctr/m/cc/transcript/stocker.pdf>
- 753 Joseph PV, Srinivasan J (1999) Rossby waves in May and the Indian summer mon-  
754 soon rainfall. Tellus A 51(5):854–864, DOI 10.1034/j.1600-0870.1999.00021.x, URL  
755 <http://tellusa.net/index.php/tellusa/article/view/14497>
- 756 Joshi MM, Gregory JM, Webb MJ, Sexton DMH, Johns TC (2008) Mech-  
757 anisms for the land/sea warming contrast exhibited by simulations of cli-

- 758 mate change. *Clim Dyn* 30(5):455–465, DOI 10.1007/s00382-007-0306-1, URL  
759 <http://link.springer.com/10.1007/s00382-007-0306-1>
- 760 Kamae Y, Shiogama H, Watanabe M, Kimoto M (2014a) Attributing the increase in North-  
761 ern Hemisphere hot summers since the late 20th century. *Geophys Res Lett* 41(14):5192–  
762 5199, DOI 10.1002/2014GL061062, URL <http://doi.wiley.com/10.1002/2014GL061062>
- 763 Kamae Y, Watanabe M, Kimoto M, Shiogama H (2014b) Summertime land-sea thermal  
764 contrast and atmospheric circulation over East Asia in a warming climate-Part II: Im-  
765 portance of CO<sub>2</sub>-induced continental warming. *Clim Dyn* 43(9-10):2569–2583, DOI  
766 10.1007/s00382-014-2146-0, URL <http://link.springer.com/10.1007/s00382-014-2146-0>
- 767 Krishnamurti TN, Stefanova L, Misra V (2013) Tropical Meteorology: An Introduction.  
768 Springer
- 769 Lambert FH, Webb MJ, Joshi MM (2011) The Relationship be-  
770 tween Land-Ocean Surface Temperature Contrast and Radiative Forc-  
771 ing. *J Clim* 24(13):3239–3256, DOI 10.1175/2011JCLI3893.1, URL  
772 <http://journals.ametsoc.org/doi/abs/10.1175/2011JCLI3893.1>
- 773 Lee MH, Lee S, Song HJ, Ho CH (2017) The recent increase in the occur-  
774 rence of a boreal summer teleconnection and its relationship with temperature  
775 extremes. *J Clim* pp JCLI-D-16-0094.1, DOI 10.1175/JCLI-D-16-0094.1, URL  
776 <http://journals.ametsoc.org/doi/10.1175/JCLI-D-16-0094.1>
- 777 Lin H (2009) Global Extratropical Response to Diabatic Heating Variability of the Asian  
778 Summer Monsoon. *J Atmos Sci* 66(9):2697–2713, DOI 10.1175/2009JAS3008.1, URL  
779 <http://journals.ametsoc.org/doi/abs/10.1175/2009JAS3008.1>
- 780 Manola I, Selten F, de Vries H, Hazeleger W (2013) “Waveguidability” of idealized  
781 jets. *J Geophys Res Atmos* 118(18):10,432–10,440, DOI 10.1002/jgrd.50758, URL  
782 <http://doi.wiley.com/10.1002/jgrd.50758>

- 783 Millar RJ, Fuglestvedt JS, Friedlingstein P, Rogelj J, Grubb MJ, Matthews HD, Skeie  
784 RB, Forster PM, Frame DJ, Allen MR (2017) Emission budgets and pathways con-  
785 sistent with limiting warming to 1.5C. *Nat Geosci* DOI 10.1038/ngeo3031, URL  
786 <http://www.nature.com/doifinder/10.1038/ngeo3031>
- 787 Mitchell D, AchutaRao K, Allen M, Bethke I, Forster P, Fuglestvedt J, Gillett N, Haustein K,  
788 Iverson T, Massey N, Schleussner CF, Scinocca J, Selander Ø, Shiogama H, Shuckburgh E,  
789 Sparrow S, Stone D, Wallom D, Wehner M, Zaaboul R (2017) Half a degree Additional  
790 warming, Projections, Prognosis and Impacts (HAPPI): Background and Experimental  
791 Design. *Geosci Model Dev Discuss* 10(2):571–583, DOI 10.5194/gmd-2016-203, URL  
792 <http://www.geosci-model-dev-discuss.net/gmd-2016-203/>
- 793 Mitchell JFB (1983) The seasonal response of a general circulation model to changes  
794 in CO<sub>2</sub> and sea temperatures. *Q J R Meteorol Soc* 109(459):113–152, DOI  
795 10.1002/qj.49710945906, URL <http://doi.wiley.com/10.1002/qj.49710945906>
- 796 O'Reilly CH, Woollings T, Zanna L, Weisheimer A (2018) The impact of trop-  
797 ical precipitation on summertime Euro-Atlantic circulation via a circumglobal  
798 wave-train. *J Clim* pp JCLI-D-17-0451.1, DOI 10.1175/JCLI-D-17-0451.1, URL  
799 <http://journals.ametsoc.org/doi/10.1175/JCLI-D-17-0451.1>
- 800 Petoukhov V, Rahmstorf S, Petri S, Schellnhuber HJ (2013) Quasireso-  
801 nant amplification of planetary waves and recent Northern Hemisphere  
802 weather extremes. *Proc Natl Acad Sci U S A* 110(14):5336–41, DOI  
803 10.1073/pnas.1222000110, URL <http://www.ncbi.nlm.nih.gov/pubmed/23457264>  
804 <http://www.pubmedcentral.nih.gov/articlerender.fcgi?artid=PMC3619331>
- 805 Pope VD, Gallani ML, Rowntree PR, Stratton RA (2000) The impact  
806 of new physical parametrizations in the Hadley Centre climate model:  
807 HadAM3. *Clim Dyn* 16(2-3):123–146, DOI 10.1007/s003820050009, URL

- 808        <http://link.springer.com/10.1007/s003820050009>
- 809        Richardson TB, Forster PM, Andrews T, Parker DJ (2016) Understanding the Rapid Precipi-
- 810        tation Response to CO<sub>2</sub> and Aerosol Forcing on a Regional Scale\*. J Clim 29(2):583–594,
- 811        DOI 10.1175/JCLI-D-15-0174.1, URL <http://journals.ametsoc.org/doi/10.1175/JCLI-D-15-0174.1>
- 812
- 813        Sardeshmukh PD, Hoskins BJ (1988) The Generation of Global Rota-
- 814        tional Flow by Steady Idealized Tropical Divergence. J Atmos Sci
- 815        45(7):1228–1251, DOI 10.1175/1520-0469(1988)045;1228:TGOGRF;2.0.CO;2,
- 816        URL <http://journals.ametsoc.org/doi/abs/10.1175/1520-0469%281988%29045%3C1228%3ATGOGRF%3E2.0.CO%3B2>
- 817
- 818        Schaller N, Kay AL, Lamb R, Massey NR, van Oldenborgh GJ, Otto FEL, Sparrow SN, Vau-
- 819        tard R, Yiou P, Ashpole I, Bowery A, Crooks SM, Haustein K, Huntingford C, Ingram
- 820        WJ, Jones RG, Legg T, Miller J, Skeggs J, Wallom D, Weisheimer A, Wilson S, Stott
- 821        PA, Allen MR (2016) Human influence on climate in the 2014 southern England win-
- 822        ter floods and their impacts. Nat Clim Chang 6(6):627–634, DOI 10.1038/nclimate2927,
- 823        URL <http://www.nature.com/articles/nclimate2927>
- 824        Schubert S, Wang H, Suarez M (2011) Warm Season Subseasonal Variability
- 825        and Climate Extremes in the Northern Hemisphere: The Role of Stationary
- 826        Rossby Waves. J Clim 24(18):4773–4792, DOI 10.1175/JCLI-D-10-05035.1, URL
- 827        <http://journals.ametsoc.org/doi/abs/10.1175/JCLI-D-10-05035.1>
- 828        Screen JA, Simmonds I (2014) Amplified mid-latitude planetary waves favour particular
- 829        regional weather extremes. Nat Clim Chang 4(8):704–709, DOI 10.1038/nclimate2271,
- 830        URL <http://www.nature.com/doifinder/10.1038/nclimate2271>
- 831        Seager R, Naik N, Vecchi GA (2010) Thermodynamic and Dynamic Mecha-
- 832        nisms for Large-Scale Changes in the Hydrological Cycle in Response to

- 833 Global Warming\*. *J Clim* 23(17):4651–4668, DOI 10.1175/2010JCLI3655.1, URL  
834 <http://journals.ametsoc.org/doi/abs/10.1175/2010JCLI3655.1>
- 835 Seneviratne SI, Donat MG, Mueller B, Alexander LV (2014) No pause in the increase of hot  
836 temperature extremes. *Nat Clim Chang* 4(3):161–163, DOI 10.1038/nclimate2145, URL  
837 <http://www.nature.com/doifinder/10.1038/nclimate2145>
- 838 Sexton DMH, Grubb H, Shine KP, Folland CK (2003) Design and Analy-  
839 sis of Climate Model Experiments for the Efficient Estimation of Anthro-  
840 pogenic Signals. *J Clim* 16(9):1320–1336, DOI 10.1175/1520-0442-16.9.1320, URL  
841 <http://journals.ametsoc.org/doi/abs/10.1175/1520-0442-16.9.1320>
- 842 Shaw TA, Voigt A (2015) Tug of war on summertime circulation between radiative forc-  
843 ing and sea surface warming. *Nat Geosci* 8(7):560–566, DOI 10.1038/ngeo2449, URL  
844 <http://www.nature.com/doifinder/10.1038/ngeo2449>
- 845 Simpson IR, Shaw TA, Seager R (2014) A Diagnosis of the Seasonally and  
846 Longitudinally Varying Midlatitude Circulation Response to Global Warm-  
847 ing\*. *J Atmos Sci* 71(7):2489–2515, DOI 10.1175/JAS-D-13-0325.1, URL  
848 <http://journals.ametsoc.org/doi/abs/10.1175/JAS-D-13-0325.1>
- 849 Simpson IR, Seager R, Ting M, Shaw TA (2016) Causes of change in North-  
850 ern Hemisphere winter meridional winds and regional hydroclimate. *Nat Clim  
851 Chang* 6:65–70, DOI 10.1175/1520-0469(1986)043;2944:LSOTSE;2.0.CO;2, URL  
852 <http://www.nature.com/nclimate/journal/v6/n1/full/nclimate2783.html>
- 853 Skinner CB, Ashfaq M, Diffenbaugh NS (2012) Influence of Twenty-First-  
854 Century Atmospheric and Sea Surface Temperature Forcing on West  
855 African Climate. *J Clim* 25(2):527–542, DOI 10.1175/2011JCLI4183.1, URL  
856 <http://journals.ametsoc.org/doi/abs/10.1175/2011JCLI4183.1>

- 857 Sugi M, Yoshimura J (2004) A Mechanism of Tropical Pre-  
858 cipitation Change due to CO<sub>2</sub> Increase. *J Clim* 17(1):238–  
859 243, DOI 10.1175/1520-0442(2004)017j0238:AMOTPC;2.0.CO;2,  
860 URL <http://journals.ametsoc.org/doi/abs/10.1175/1520-0442%282004%29017%3C0238%3AAMOTPC%3E2.0.CO%3B2>
- 861
- 862 Taylor KE, Stouffer RJ, Meehl GA (2012) An Overview of CMIP5 and the Experiment De-  
863 sign. *Bull Am Meteorol Soc* 93(4):485–498, DOI 10.1175/BAMS-D-11-00094.1, URL  
864 <http://journals.ametsoc.org/doi/abs/10.1175/BAMS-D-11-00094.1>
- 865 Ting M (1994) Maintenance of Northern Summer Stationary Waves in a GCM. *J Atmos Sci*  
866 51(22):3286–3308, DOI 10.1175/1520-0469(1994)051j3286:MONSSW;2.0.CO;2,  
867 URL <http://journals.ametsoc.org/doi/abs/10.1175/1520-0469%281994%29051%3C3286%3AMONSSW%3E2.0.CO%3B2>
- 868
- 869 Voigt A, Shaw TA (2015) Circulation response to warming shaped by radiative changes  
870 of clouds and water vapour. *Nat Geosci* 8(2):102–106, DOI 10.1038/ngeo2345, URL  
871 <http://www.nature.com/doifinder/10.1038/ngeo2345>
- 872 Watanabe M, Suzuki T, O’ishi R, Komuro Y, Watanabe S, Emori S, Takemura T, Chikira M,  
873 Ogura T, Sekiguchi M, Takata K, Yamazaki D, Yokohata T, Nozawa T, Hasumi H, Tatebe  
874 H, Kimoto M (2010) Improved Climate Simulation by MIROC5: Mean States, Variability,  
875 and Climate Sensitivity. *J Clim* 23(23):6312–6335, DOI 10.1175/2010JCLI3679.1, URL  
876 <http://journals.ametsoc.org/doi/abs/10.1175/2010JCLI3679.1>
- 877 Webb MJ, Andrews T, Bodas-Salcedo A, Bony S, Bretherton CS, Chadwick R, Chepfer H,  
878 Douville H, Good P, Kay JE, Klein SA, Marchand R, Medeiros B, Siebesma AP, Skin-  
879 ner CB, Stevens B, Tselioudis G, Tsushima Y, Watanabe M (2017) The Cloud Feed-  
880 back Model Intercomparison Project (CFMIP) contribution to CMIP6. *Geosci Model  
881 Dev* 10(1):359–384, DOI 10.5194/gmd-10-359-2017, URL <https://www.geosci-model-dev.net/10/359/2017/>

882 dev.net/10/359/2017/

883 Wulff CO, Greatbatch RJ, Domeisen DI, Gollan G, Hansen F (2017) Tropical forcing of  
884 the Summer East Atlantic pattern. *Geophys Res Lett* DOI 10.1002/2017GL075493, URL  
885 <http://doi.wiley.com/10.1002/2017GL075493>

886 Yasui S, Watanabe M (2010) Forcing Processes of the Sum-  
887 mertime Circumglobal Teleconnection Pattern in a Dry AGCM.  
888 *J Clim* 23(8):2093–2114, DOI 10.1175/2009JCLI3323.1, URL  
889 <http://journals.ametsoc.org/doi/abs/10.1175/2009JCLI3323.1>